A framework based on 2-D Taylor expansion for quantifying the impacts of sub-pixel reflectance variance and covariance on cloud optical thickness and effective radius retrievals based on the bi-spectral method

Z. Zhang[1,2,*], F. Werner[2], H.-M. Cho[2,3], G. Wind,[4,5]
S. Platnick[4], A. S. Ackerman[6], L. Di Girolamo[7], and A. Marshak[4], Kerry Meyer[4,8]

1. Physics Department, UMBC, Baltimore, MD, USA
2. Joint Center for Earth Systems Technology, UMBC, Baltimore, MD, USA
3. Electronics and Telecommunications Research Institute, Korea
4. NASA Goddard Space Flight Center, Greenbelt, MD, USA
5. Science Systems and Applications, Inc., Maryland 20706, USA
6. NASA Goddard Institute for Space Studies, New York City, NY, USA
7. Department of Atmospheric Sciences, University of Illinois, Urbana-Champaign, IL, USA
8. Universities Space Research Association (USRA), Columbia, MD, USA

*Corresponding author: Zhibo Zhang
Email: Zhibo.Zhang@umbc.edu

1   **Abstract:**

2   The bi-spectral method retrieves cloud optical thickness (τ) and cloud droplet

3   effective radius (r_e) simultaneously from a pair of cloud reflectance observations, one in

4   a visible or near infrared (VIS/NIR) band and the other in a shortwave-infrared (SWIR)

5   band. A cloudy pixel is usually assumed to be horizontally homogeneous in the retrieval.

6   Ignoring sub-pixel variations of cloud reflectances can lead to a significant bias in the

7   retrieved τ and r_e. In the literature, the retrievals of τ and r_e are often assumed to be

8   independent and considered separately when investigating the impact of sub-pixel

9   cloud reflectance variations on the bi-spectral method. As a result, the impact on τ is

10   contributed only by the sub-pixel variation of VIS/NIR band reflectance and the impact

11   on r_e only by the sub-pixel variation of SWIR band reflectance.

12   In our new framework, we use the Taylor expansion of a two-variable function to

13   understand and quantify the impacts of sub-pixel variances of VIS/NIR and SWIR cloud

14   reflectances and their covariance on the τ and r_e retrievals. This framework takes into

15   account the fact that the retrievals are determined by both VIS/NIR and SWIR band

16   observations in a mutually dependent way. In comparison with previous studies, it

17   provides a more comprehensive understanding of how sub-pixel cloud reflectance

18   variations impact the τ and r_e retrievals based on the bi-spectral method. In particular,

19   our framework provides a mathematical explanation of how the sub-pixel variation in

20   VIS/NIR band influences the r_e retrieval and why it can sometimes outweigh the

21   influence of variations in the SWIR band and dominate the error in r_e retrievals, leading

22   to a potential contribution of positive bias to the r_e retrieval. We test our framework

23   using synthetic cloud fields from a large-eddy simulation and real observations from

24   MODIS. The predicted results based on our framework agree very well with the

25   numerical simulations. Our framework can be used to estimate the retrieval uncertainty

26   from sub-pixel reflectance variations in operational satellite cloud products and to help

27   understand the differences in τ and r_e retrievals between two instruments.

28

29

1. Introduction

Among many satellite-based cloud remote sensing techniques, the bi-spectral solar reflective method ("bi-spectral method" hereafter) is a widely used method to infer cloud optical thickness (τ) and cloud droplet effective radius (r_e) from satellite observation of cloud reflectance [*Nakajima and King*, 1990]. This method uses cloud reflectance measurements from two spectral bands to simultaneously retrieve τ and r_e. One measurement is usually made in the visible or near-infrared (VIS/NIR) spectral region (e.g., 0.64 µm or 0.86 µm), where water absorption is negligible and therefore cloud reflection generally increases with τ. The other measurement is usually in the shortwave infrared (SWIR) spectral region (e.g., 2.1 µm or 3.7 µm), where water drops are moderately absorptive and cloud reflectance generally decreases with increasing r_e for optically thick clouds. In practice, the bi-spectral method is often implemented utilizing the so-called look-up-table (LUT). A couple of LUT examples are shown in Figure 1. Such LUTs contain pre-computed bi-directional cloud reflectances at VIS/NIR and SWIR bands for various combinations of r_e and τ under different sun-satellite viewing geometries and surface reflectances. Given the observed reflectances, the corresponding r_e and τ can be retrieved easily by searching and interpolating the proper LUT. The bi-spectral method has been adopted by a number of satellite missions, including Moderate Resolution Imaging Spectroradiometer (MODIS), Visible Infrared Imaging Radiometer Suite (VIIRS), and Spinning Enhanced Visible and Infrared Imager (SEVIRI) for operational retrievals of cloud properties (i.e., τ, r_e and derived cloud liquid

51   water path (LWP)) [*Platnick et al.*, 2003; *Roebeling et al.*, 2006; *Minnis et al.*, 2011;

52   *Walther and Heidinger*, 2012]. Given the wide usage of the bi-spectral method, it is

53   critical to study and understand its limitations and uncertainties.

54   The bi-spectral method makes several important assumptions about the cloud

55   (or cloudy pixels). First, within a cloudy pixel, cloud is assumed to be horizontally

56   homogenous (referred to as the "homogenous pixel assumption"). Second, it is assumed

57   that the pixels are independent from each other, in the sense that there is no net inter-

58   pixel transport of radiation (often referred to as the "independent pixel assumption,

59   IPA"). Under these assumptions, clouds are considered to be "plane-parallel". In

60   addition to plane-parallel cloud assumptions, clouds are often assumed to be vertically

61   homogenous in the operational algorithms. Furthermore, the size spectrum of cloud

62   particles is often assumed to follow certain analytical distributions, such as the single

63   modal gamma or lognormal size distributions [e.g., *Nakajima and King*, 1990; *Dong et*

64   *al.*, 1997]. These assumptions may be reasonable for certain types of clouds, such as

65   closed-cell, non-precipitating stratocumulus, but become problematic for others, such

66   as broken trade-wind cumuli or precipitating clouds [*Di Girolamo et al.*, 2010; *Painemal*

67   *and Zuidema*, 2011; *Zhang and Platnick*, 2011; *Liang and Girolamo*, 2013; *Zhang*, 2013].

68   As elucidated in numerous previous studies, when real clouds deviate from these

69   assumptions, the r_e and τ retrievals from the bi-spectral method can suffer from large

70   errors and uncertainties [e.g., *Várnai and Marshak*, 2002; *Kato et al.*, 2006; *Marshak et*

71   *al.*, 2006; *Zhang and Platnick*, 2011; *Zhang et al.*, 2012; *Zhang*, 2013; *Liang et al.*, 2015].

72   The focus of this study is the homogenous pixel assumption. Our objective is to

73   develop a unified framework for understanding and quantifying the impacts of sub-pixel

74   level unresolved reflectance variations on r_e and τ retrievals based on the bi-spectral

75   method. A number of previous studies have already made substantial progress in this

76   direction. It has been known for a long time that at the spatial scale of climate model

77   grids (e.g., ~ 10^2 km) approximating inhomogeneous cloud fields with plane-parallel

78   clouds can lead to significant biases in shortwave solar radiation [e.g., *Harshvardhan*

79   *and Randall*, 1985; *Cahalan et al.*, 1994; *Barker*, 1996]. *Cahalan et al.* [1994] described

80   an elegant theoretical framework based on a fractal cloud model to explain the

81   influence of small-scale horizontal variability of τ on the averaged cloud reflectance in

82   the visible spectral region R_{VIS}. It is shown that the averaged reflectance $\overline{R_{VIS}(\tau_i)}$,

83   where τ_i denotes the sub-pixel scale cloud optical thickness, is smaller than the

84   reflectance that corresponds to the averaged cloud optical thickness $\overline{\tau_i}$, i.e.,

85    $\overline{R_{VIS}(\tau_i)} < R_{VIS}(\overline{\tau_i})$. This inequality relation is well known as the "plane-parallel

86   homogenous bias" (referred to as PPHB), which is a result of the non-linear dependence

87   of R_{VIS} on τ i.e., $\dfrac{\partial^2 R_{vis}}{\partial \tau^2} < 0$. The implication of the PPHB for τ retrievals from R_{VIS} is

88   illustrated using an example shown in Figure 2a. Here, we assume that one half of an

89   inhomogeneous pixel is covered by a thinner cloud with $\tau_1 = 5$ and the other half by a

90   thicker cloud with $\tau_2 = 18$ (both clouds with $r_e = 8\mu m$). Because of the PPHB, the

91   retrieved cloud optical thickness $\tau^* = 9.8$ based on the averaged reflectance

4

92   $\bar{R} = \left[R(\tau_1) + R(\tau_2) \right]/2$ is significantly smaller than the linear average of the sub-pixel τ,

93   i.e., $\bar{\tau} = 11.5$. The impacts of PPHB on satellite based cloud property retrievals and the

94   implications have been investigated in a number of studies [*Oreopoulos and Davies*,

95   1998; *Pincus et al.*, 1999; *Oreopoulos et al.*, 2007].

96   We note that the variation of cloud reflectance may be a result of varying cloud

97   properties, but may also be caused by 3-D radiative effects. For example, a cloudy pixel

98   can be perfectly homogenous in terms of cloud properties, but the surrounding pixels

99   can cast a shadow on part of this pixel leading to sub-pixel reflectance variation

100   [*Marshak et al.*, 2006]. A variety of such 3-D effects that cannot be explained by the 1-D

101   plane-parallel radiative transfer theory have been identified and their impacts on cloud

102   property retrievals investigated in previous studies [*Davis and Marshak*, 2010]. In

103   reality, the PPHB is inevitably entangled with the 3-D transfer effects and other

104   uncertainties such as the impact of instrument noise in the retrieval. It is difficult, if not

105   impossible, to separate them. Following the literature, we shall refer to the impact of

106   sub-pixel cloud reflectance variation on cloud property retrievals as the PPHB, while

107   keeping in mind that the sub-pixel cloud reflectance variation can also result from 3-D

108   radiative effects and may not reflect the true variation of sub-pixel cloud properties.

109   Recently, as the interests in aerosol-cloud interactions have grown, there is an

110   increasing attention on the impacts of small-scale cloud variations on the satellite-based

111   r_e retrievals [e.g., *Kato et al.*, 2006; *Marshak et al.*, 2006; *Zhang and Platnick*, 2011;

112   *Zhang et al.*, 2012; *Liang et al.*, 2015]. Marshak et al. [2006] pointed out that similar to

113   the PPHB the non-linear dependence of the SWIR band cloud reflectance R_{SWIR} on r_e

114 can also lead to significant biases on r_e retrievals, which is demonstrated in Figure 2b.

115 Here, one half of an inhomogeneous pixel is covered by a cloud with $r_e = 8\mu m$ and the

116 other half by a cloud with $r_e = 22\mu m$. Both parts have the same $\tau = 4.1$. As shown in the

117 figure, the retrieved $r_e^* = 12\mu m$ based on the averaged reflectance is significantly

118 smaller than the linear average of sub-pixel $\overline{r_e} = 15\mu m$, similar to the PPHB of τ in

119 Figure 2a. It must be noted that in the framework of Marshak et al. [2006] the retrievals

120 of r_e and τ are considered separately and assumed to be independent from one

121 another. However, as Marshak et al. [2006] pointed out this assumption is valid only for

122 "large enough" τ and r_e (typically, $r_e >$ 5 μm and $\tau >$ 10). As one can see from the

123 shape of the LUT in Figure 1 the R_{SWIR} is not completely orthogonal to the R_{VIS},

124 especially when τ is small. As a result, the retrievals of r_e and τ are not independent

125 from one another. Marshak et al. [2006] suspected that some cases with large r_e bias in

126 their simulations might be the result of this mutual dependence of r_e and τ retrievals.

127 Zhang and Platnick [2011] showed that the sub-pixel variance of τ can have a significant

128 impact on the r_e retrieval, which is illustrated in the example in Figure 2c. In this

129 hypothetical case, an inhomogeneous pixel is assumed to be covered by a thinner cloud

130 with τ_1=6 in one half and a thicker cloud with τ_2=18 in the other. Both clouds have the

131 same r_e=14 μm. Note that in this case the sub-pixel reflectance variation is solely caused

132 by the variability in τ. If the r_e retrieval were independent from the τ retrieval, then the

133 retrieved r_e would be 14 μm. The solid triangle in the figure indicates the location of the

134 R_{VIS} and R_{SWIR} averaged over the pixel, i.e., the "observation". The retrieved $\tau^* = 10.8$

135 is smaller than the averaged $\bar{\tau} = 12$ as a result of the PPHB. However, the retrieved

136 $r_e^* = 16$ is 2 μm larger than the expected value of 14 μm. This positive bias in the r_e

137 retrieval, apparently caused by the sub-pixel variability of τ , cannot be explained by the

138 framework of Marshak et al. [2006] in which the r_e retrieval is assumed to be

139 independent from the τ retrieval. Zhang and Platnick [2011] and Zhang et al. [2012] also

140 found that the magnitude of the positive r_e retrieval bias caused by the sub-pixel

141 variability of τ is dependent on the SWIR band chosen for the r_e retrieval. These studies

142 showed that the same sub-pixel τ variability tends to induce larger bias in retrieved r_e

143 using the less absorptive 2.1 μm band (referred to as $r_{e,2.1}$) than that using the more

144 absorptive 3.7 μm band (referred to as $r_{e,3.7}$). This spectral dependence provides an

145 important explanation for the fact that the MODIS operational $r_{e,2.1}$ retrievals for water

146 clouds are often significantly larger than the $r_{e,3.7}$ retrievals, especially when clouds have

147 large sub-pixel heterogeneity [*Zhang and Platnick*, 2011; *Cho et al.*, 2015].

148 The aforementioned studies have undoubtedly shed important light on the

149 impact of sub-pixel cloud variability on r_e and τ retrievals based on the bi-spectral

150 method. However, several questions still remain. For example, an important question is

151 how to reconcile the negative r_e bias discussed in Marshak et al. [*Marshak et al.*, 2006]

152 and the positive r_e bias discussed in Zhang and Platnick [2011] and Zhang et al. [2012].

153 Indeed, this is the main question we will address in this study. In the light of previous

154 studies, here we develop a new mathematical framework to provide a more

155 comprehensive and complete understanding of the impact of sub-pixel cloud variability

156 on r_e and τ retrievals based on the bi-spectral method. The paper is organized as

157 follows: We formulate the problem in Section 2. We introduce our mathematical

158 framework in Section 3, test and validate it using two examples in Section 4, and discuss

159 its applications in Section 5.

160 ## 2. Statement of the problem

161 In the bi-spectral method, r_e and τ are retrieved from a pair of cloud reflectance

162 observations, one in VIS/NIR and the other in SWIR. From this point of view, we can

163 define r_e and τ as:

164
$$\begin{aligned} \tau &\equiv \tau\left(R_{VIS}, R_{SWIR}\right) \\ r_e &\equiv r_e\left(R_{VIS}, R_{SWIR}\right) \end{aligned},$$
(1)

165 where R_{VIS} and R_{SWIR} are the observed reflectances in the VIS/NIR (denoted by

166 subscript "VIS" for short) and SWIR bands, respectively. Assume that an instrument with

167 a relatively coarse spatial resolution observes a horizontally inhomogeneous cloudy

168 pixel in its field of view. The observed cloud reflectances are $\overline{R_{VIS}}$ and $\overline{R_{SWIR}}$, where the

169 overbar denotes the spatial average. Now if we use another instrument with a finer

170 spatial resolution to observe the same area covered by the coarser resolution pixel, we

171 can obtain high-resolution observations, $R_{VIS,i}$ and $R_{SWIR,i}, i = 1, 2, ...N$, (the number N

172 depends on the relative sizes of the pixels). The high-resolution measurements provide

173 the information on the variance and covariance of R_{VIS} and R_{SWIR} at sub-pixel scale.

174 Each sub-pixel observation $R_{VIS,i}$ and $R_{SWIR,i}$ can be specified as the deviation from the

175 mean value $\overline{R_{VIS}}$ and $\overline{R_{SWIR}}$ as:

8

$$R_{VIS,i} = \overline{R_{VIS}} + \Delta R_{VIS,i}$$
$$R_{SWIR,i} = \overline{R_{SWIR}} + \Delta R_{SWIR,i} \quad ; i = 1,2...N \,.$$
(2)

177 It naturally follows that the spatial average $\overline{\Delta R_{VIS,i}} = \overline{\Delta R_{SWIR,i}} = 0$. Based on the coarse-

178 resolution reflectance observations $\overline{R_{VIS}}$ and $\overline{R_{SWIR}}$, we can retrieve $\tau\left(\overline{R_{VIS}}, \overline{R_{SWIR}}\right)$ and

179 $r_e\left(\overline{R_{VIS}}, \overline{R_{SWIR}}\right)$. From the high-resolution, sub-pixel observations $R_{VIS,i}$ and $R_{SWIR,i}$, we can

180 retrieve $\tau\left(R_{VIS,i}, R_{SWIR,i}\right)$ and $r_e\left(R_{VIS,i}, R_{SWIR,i}\right)$. The differences $\Delta\tau$ and Δr_e, defined as:

$$\Delta\tau = \tau\left(\overline{R_{VIS}}, \overline{R_{SWIR}}\right) - \overline{\tau\left(R_{VIS,i}, R_{SWIR,i}\right)}$$
$$\Delta r_e = r_e\left(\overline{R_{VIS}}, \overline{R_{SWIR}}\right) - \overline{r_e\left(R_{VIS,i}, R_{SWIR,i}\right)} \,,$$
(3)

182 are considered in this, as well as previous studies, as the biases caused by the

183 homogeneous pixel assumption in r_e and τ retrievals [*Cahalan and Joseph*, 1989;

184 *Marshak et al.*, 2006; *Zhang et al.*, 2012].

185 Consideration of eq. (3) raises a few important questions. What are the sign and

186 magnitude of $\Delta\tau$ and Δr_e? How do they depend on the sub-pixel $R_{VIS,i}$ and $R_{SWIR,i}$?

187 Addressing these questions could help improve understanding of the biases caused by

188 ignoring the sub-pixel reflectance variation in bi-spectral r_e and τ retrievals.

189 Furthermore, since performing high-resolution retrievals can be computationally

190 expensive, another important question is whether it is possible to estimate

191 $\overline{\tau\left(R_{VIS,i}, R_{SWIR,i}\right)}$ and $\overline{r_e\left(R_{VIS,i}, R_{SWIR,i}\right)}$ from the coarse-resolution retrievals and the

192 statistics of sub-pixel reflectance observations, even without doing time-consuming

193 high-resolution retrievals. If this proved possible, then it is a very efficient way to

194   estimate the biases and uncertainty caused by the homogenous pixel assumption. These

195   questions are the focus of this study and will be addressed in the next section.

196   Before proceeding, we need to clarify two points. First, the $\Delta\tau$ and Δr_e in Eq. (3)

197   are the differences between two sets of retrievals, *not* the differences between the

198   retrievals and "true" cloud properties. As aforementioned, sub-pixel reflectance

199   variations can be due to sub-pixel scale cloud property variation, but may also be caused

200   by 3-D radiative effects. If the former is dominant, then $\Delta\tau$ and Δr_e provide an

201   estimate of the PPHB and can be used to correct the coarse-resolution retrievals to

202   better represent the "true" cloud properties. However, if 3-D effects are the dominant

203   cause of the sub-pixel reflectance variation, then $\Delta\tau$ and Δr_e can be considered a

204   quantitative index of the 3-D effects on the retrievals. Second, our scope is to study the

205   connections between retrieval biases $\Delta\tau$ and Δr_e with sub-pixel observations $R_{VIS,i}$

206   and $R_{SWIR,i}$. We simply take $R_{VIS,i}$ and $R_{SWIR,i}$ as given inputs. Here we do *not* seek to

207   explain the characteristics of $R_{VIS,i}$ and $R_{SWIR,i}$ (e.g., their mean values, variances and

208   covariance), or their dependence on cloud properties. Neither do we try to explain how

209   the 3-D radiative effects and instrument characteristics influence $R_{VIS,i}$ and $R_{SWIR,i}$.

210

3. A unified mathematical framework

212   In this section, we will introduce a comprehensive framework that is able to

213   reconcile and unify the theoretical understandings provided by Marshak et al. [2006] ,

214   Zhang and Platnick [2011], and Zhang et al. [2012] To investigate the sign and

215   magnitude of $\Delta\tau$ and Δr_e, we first expand the $\tau\left(R_{VIS,i},R_{SWIR,i}\right)$ and $r_e\left(R_{VIS,i},R_{SWIR,i}\right)$ into

216   two-dimensional Taylor series of $R_{VIS,i}$ and $R_{SWIR,i}$. Take $r_e\left(R_{VIS,i},R_{SWIR,i}\right)$ for example.

217   The expansion is:

218

$$
\begin{aligned}
r_e\left(R_{VIS,i},R_{SWIR,i}\right) &= r_e\left(\overline{R_{VIS}}+\Delta R_{VIS,i},\overline{R_{SWIR}}+\Delta R_{SWIR,i}\right) \\
&= r_e\left(\overline{R_{VIS}},\overline{R_{SWIR}}\right)+\underbrace{\frac{\partial r_e\left(\overline{R_{VIS}},\overline{R_{SWIR}}\right)}{\partial R_{VIS}}\Delta R_{VIS,i}+\frac{\partial r_e\left(\overline{R_{VIS}},\overline{R_{SWIR}}\right)}{\partial R_{SWIR}}\Delta R_{SWIR,i}}_{\text{Linear terms}}+ \\
&\underbrace{\frac{1}{2}\frac{\partial^2 r_e\left(\overline{R_{VIS}},\overline{R_{SWIR}}\right)}{\partial R_{VIS}^2}\Delta R_{VIS,i}^2+\frac{\partial^2 r_e\left(\overline{R_{VIS}},\overline{R_{SWIR}}\right)}{\partial R_{VIS}\,\partial R_{SWIR}}\Delta R_{VIS,i}\Delta R_{SWIR,i}+\frac{1}{2}\frac{\partial^2 r_e\left(\overline{R_{VIS}},\overline{R_{SWIR}}\right)}{\partial R_{SWIR}^2}\Delta R_{SWIR,i}^2}_{\text{Second-order terms}}+\varepsilon
\end{aligned}
$$. (4)

219   where ε is the truncation error if higher order derivative terms are neglected. If we

220   take the spatial average of Eq. (4) and neglect ε, all the linear terms (i.e.,

221     $\dfrac{\partial r_e\left(\overline{R_{VIS}},\overline{R_{SWIR}}\right)}{\partial R_{VIS}}\Delta R_{VIS,i}$ and $\dfrac{\partial r_e\left(\overline{R_{VIS}},\overline{R_{SWIR}}\right)}{\partial R_{SWIR}}\Delta R_{SWIR,i}$) vanish because $\overline{\Delta R_{VIS,i}}=\overline{\Delta R_{SWIR,i}}=0$. Thus,

222   only second order terms in Eq. (4) remain after the spatial average:

223     $\overline{r_e\left(R_{VIS,i},R_{SWIR,i}\right)}\approx r_e\left(\overline{R_{VIS}},\overline{R_{SWIR}}\right)+\dfrac{1}{2}\dfrac{\partial^2 r_e\left(\overline{R_{VIS}},\overline{R_{SWIR}}\right)}{\partial R_{VIS}^2}\sigma_{VIS}^2+\dfrac{\partial^2 r_e\left(\overline{R_{VIS}},\overline{R_{SWIR}}\right)}{\partial R_{VIS}\,\partial R_{SWIR}}\mathrm{cov}\left(R_{VIS},R_{SWIR}\right)+\dfrac{1}{2}\dfrac{\partial^2 r_e\left(\overline{R_{VIS}},\overline{R_{SWIR}}\right)}{\partial R_{SWIR}^2}\sigma_{SWIR}^2$,

224   (5)

225   where $\sigma_{VIS}^2=\overline{\Delta R_{VIS,i}^2}$, $\sigma_{SWIR}^2=\overline{\Delta R_{SWIR,i}^2}$ are the spatial variances of $R_{VIS,i}$ and $R_{SWIR,i}$,

226   respectively, and $\mathrm{cov}\left(R_{VIS},R_{SWIR}\right)$ is the spatial covariance of $R_{VIS,i}$ and $R_{SWIR,i}$.

227   Substituting Eq. (5) into Eq. (3), we obtain the following formula for Δr_e:

228

$$\Delta r_e = r_e \left(\overline{R_{VIS}}, \overline{R_{SWIR}} \right) - \overline{r_e \left(R_{VIS,i}, R_{SWIR,i} \right)}$$

$$= -\frac{1}{2} \frac{\partial^2 r_e \left(\overline{R_{VIS}}, \overline{R_{SWIR}} \right)}{\partial R_{VIS}^2} \sigma_{VIS}^2 - \frac{\partial^2 r_e \left(\overline{R_{VIS}}, \overline{R_{SWIR}} \right)}{\partial R_{VIS} \partial R_{SWIR}} \mathrm{cov} \left(R_{VIS}, R_{SWIR} \right) - \frac{1}{2} \frac{\partial^2 r_e \left(\overline{R_{VIS}}, \overline{R_{SWIR}} \right)}{\partial R_{SWIR}^2} \sigma_{SWIR}^2 \, .$$

229 $\hspace{7cm}$ (6)

230 Following the same procedure, we can derive the formula for $\Delta \tau$ as:

231

$$\Delta \tau = \tau \left(\overline{R_{VIS}}, \overline{R_{SWIR}} \right) - \overline{\tau \left(R_{VIS,i}, R_{SWIR,i} \right)}$$

$$= -\frac{1}{2} \frac{\partial^2 \tau \left(\overline{R_{VIS}}, \overline{R_{SWIR}} \right)}{\partial R_{VIS}^2} \sigma_{VIS}^2 - \frac{\partial^2 \tau \left(\overline{R_{VIS}}, \overline{R_{SWIR}} \right)}{\partial R_{VIS} \partial R_{SWIR}} \mathrm{cov} \left(R_{VIS}, R_{SWIR} \right) - \frac{1}{2} \frac{\partial^2 \tau \left(\overline{R_{VIS}}, \overline{R_{SWIR}} \right)}{\partial R_{SWIR}^2} \sigma_{SWIR}^2 \, .$$

232 $\hspace{7cm}$ (7)

233 Eq. (6) and (7) can be combined into a matrix form as follows:

234

$$\begin{pmatrix} \Delta \tau \\ \Delta r_e \end{pmatrix} = \begin{pmatrix} -\dfrac{1}{2} \dfrac{\partial^2 \tau \left(\overline{R_{VIS}}, \overline{R_{SWIR}} \right)}{\partial R_{VIS}^2} & -\dfrac{\partial^2 \tau \left(\overline{R_{VIS}}, \overline{R_{SWIR}} \right)}{\partial R_{VIS} \partial R_{SWIR}} & -\dfrac{1}{2} \dfrac{\partial^2 \tau \left(\overline{R_{VIS}}, \overline{R_{SWIR}} \right)}{\partial R_{SWIR}^2} \\ -\dfrac{1}{2} \dfrac{\partial^2 r_e \left(\overline{R_{VIS}}, \overline{R_{SWIR}} \right)}{\partial R_{VIS}^2} & -\dfrac{\partial^2 r_e \left(\overline{R_{VIS}}, \overline{R_{SWIR}} \right)}{\partial R_{VIS} \partial R_{SWIR}} & -\dfrac{1}{2} \dfrac{\partial^2 r_e \left(\overline{R_{VIS}}, \overline{R_{SWIR}} \right)}{\partial R_{SWIR}^2} \end{pmatrix} \begin{pmatrix} \sigma_{VIS}^2 \\ \mathrm{cov} \\ \sigma_{SWIR}^2 \end{pmatrix} \, .$$

235 $\hspace{7cm}$ (8)

236 $\hspace{1cm}$ Eq. (8) is the central equation of our framework for quantifying the impact of

237 sub-pixel reflectance variance on r_e and τ retrievals. Eq. (8) decomposes the impact of

238 sub-pixel cloud reflectance variability on the τ and r_e retrievals based on the bi-spectral

239 method into two parts: 1) the magnitude of the sub-pixel reflectance variance and

240 covariance specified by the vector $\left(\sigma_{VIS}^2, \mathrm{cov}, \sigma_{SWIR}^2 \right)^T$ (referred to as "sub-pixel

241 variance vector") and 2) the matrix of the second-order derivatives of the LUT with

242 respect to R_{VIS} and R_{SWIR} (referred to as "matrix of 2$^{\text{nd}}$ derivatives"). Given the LUT, the

243 matrix of 2$^{\text{nd}}$ derivatives can be easily derived from straightforward numerical

12

244   differentiation. An example of such a derived matrix based on the LUT for 0.86 μm

245   reflectance ($R_{0.86}$) and 2.1 μm reflectance ($R_{2.1}$) is shown in Figure 3. The values of the

246   2nd derivatives for the grids of LUT are indicated by the color bar. Note that the sign of

247    $\Delta\tau$ or Δr_e is determined both by the 2nd derivatives and the sub-pixel variance vector

248    $\left(\sigma_{VIS}^2, \ \text{cov}, \ \sigma_{SWIR}^2\right)^T$. While σ_{VIS}^2 and σ_{SWIR}^2 are positive definite, the covariance term can

249   be negative.

250   It is clear from Eq. (8) that the τ and r_e retrievals are not only influenced by the

251   sub-pixel variation of the primary band (i.e., R_{VIS} for τ and R_{SWIR} for r_e) but also by the

252   variation of the secondary band (i.e., R_{SWIR} for τ and R_{VIS} for r_e), as well as the

253   covariance of the two bands R_{VIS} and R_{SWIR}. Therefore, it reconciles and unifies the

254   theoretical frameworks in Marshak et al. [2006] and Zhang and Platnick [*Zhang and*

255   *Platnick*, 2011] and Zhang et al. [2012]. In particular, the impact of the PPHB on τ and

256   r_e, described in Marshak et al. [2006], corresponds to the upper-left term,

257    $-\dfrac{1}{2}\dfrac{\partial^2 \tau\left(\overline{R_{VIS}}, \overline{R_{SWIR}}\right)}{\partial R_{VIS}^2}$ (Figure 3a), and lower-right term, $-\dfrac{1}{2}\dfrac{\partial^2 r_e\left(\overline{R_{VIS}}, \overline{R_{SWIR}}\right)}{\partial R_{SWIR}^2}$ (Figure 3f), in

258   the 2nd derivatives matrix, respectively. As shown in Figure 3, both terms are generally

259   negative over the most part of LUT, consistent with the finding of Marshak et al. [2006]

260   that ignoring sub-pixel variability tends to result in an underestimation of the pixel

261   average of the retrieved quantity if τ and r_e retrievals are considered separately and

262   independently (i.e., negative $\Delta\tau$ and Δr_e). On the other hand, $\Delta\tau$ and Δr_e are also

263   influenced by other terms in the matrix. Physically, these terms arise from the fact that

264   both R_{VIS} and R_{SWIR} depend not only on τ but also r_e. For example, the

265    $-\dfrac{1}{2}\dfrac{\partial^2 r_e\left(\overline{R_{VIS}},\overline{R_{SWIR}}\right)}{\partial R_{VIS}^2}$ term in Figure 3d is mostly positive in the region of the LUT with τ

266   between about 1.5 and 20 and r_e between about 10 and 28 µm. This term competes

267   with the negative $-\dfrac{1}{2}\dfrac{\partial^2 r_e\left(\overline{R_{VIS}},\overline{R_{SWIR}}\right)}{\partial R_{SWIR}^2}$ term in determining the sign and size of Δr_e. In

268   some cases, when σ_{VIS}^2 is large as in the example in Figure 2c, the influence of

269    $-\dfrac{1}{2}\dfrac{\partial^2 r_e\left(\overline{R_{VIS}},\overline{R_{SWIR}}\right)}{\partial R_{VIS}^2}$ may be stronger, leading to a positive Δr_e, as argued in Zhang and

270   Platnick [2011] and Zhang et al. [2012].

271   Some new terms that have not been explained in previous studies, e.g., the cross

272   terms $-\dfrac{\partial^2 \tau\left(\overline{R_{VIS}},\overline{R_{SWIR}}\right)}{\partial R_{VIS}\,\partial R_{SWIR}}$ in Figure 3b and $-\dfrac{\partial^2 r_e\left(\overline{R_{VIS}},\overline{R_{SWIR}}\right)}{\partial R_{VIS}\,\partial R_{SWIR}}$ in Figure 3e, also emerge from

273   Eq. (8). These two terms generally have the opposite sign of $-\dfrac{1}{2}\dfrac{\partial^2 \tau\left(\overline{R_{VIS}},\overline{R_{SWIR}}\right)}{\partial R_{VIS}^2}$ and

274    $-\dfrac{1}{2}\dfrac{\partial^2 r_e\left(\overline{R_{VIS}},\overline{R_{SWIR}}\right)}{\partial R_{SWIR}^2}$. Because the covariance cov is generally positive, the cross terms

275   evidently counteract the effects of $-\dfrac{1}{2}\dfrac{\partial^2 \tau\left(\overline{R_{VIS}},\overline{R_{SWIR}}\right)}{\partial R_{VIS}^2}$ and $-\dfrac{1}{2}\dfrac{\partial^2 r_e\left(\overline{R_{VIS}},\overline{R_{SWIR}}\right)}{\partial R_{SWIR}^2}$ on $\Delta\tau$

276   and Δr_e.

277   Eq. (8) also provides a quantitative explanation for why sub-pixel inhomogeneity

278   has different impacts on the r_e retrievals based on different SWIR bands (i.e., $r_{e,2.1}$ vs.

279    $r_{e,3.7}$). Figure 4 shows an example of the matrix of 2nd derivatives for the $R_{0.86}$ and $R_{3.7}$

280 combination. In comparison with the $R_{0.86}$ and $R_{2.1}$ combination in Figure 3, the

281 $-\dfrac{1}{2}\dfrac{\partial^2 r_e\left(\overline{R_{VIS}},\overline{R_{SWIR}}\right)}{\partial R_{VIS}^2}$ term in Figure 4d is significantly smaller. This suggests that the same

282 sub-pixel inhomogeneity in the 0.86 µm band (i.e., same σ_{VIS}^2) has a stronger impact on

283 $r_{e,2.1}$ than it does on $r_{e,3.7}$. Because this term tends to lead to a positive Δr_e bias, it could

284 be an important reason why the MODIS $r_{e,2.1}$ retrievals are often found to be significantly

285 larger than the $r_{e,3.7}$, in particular for inhomogeneous pixels [*Painemal and Zuidema*,

286 2011; *Zhang and Platnick*, 2011; *Zhang et al.*, 2012; *Cho et al.*, 2015].

287 　　As analyzed above, in comparison with previous studies the framework

288 described in Eq. (8) provides us with a more comprehensive explanation of the bias in τ

289 and r_e retrievals caused by the homogenous pixel assumption. This framework may be

290 useful in a variety of applications. It can be used to quantify $\Delta\tau$ and Δr_e if the sub-pixel

291 variances and covariance $\left(\sigma_{VIS}^2,\ \mathrm{cov},\ \sigma_{SWIR}^2\right)^T$ are known, as shown in the example in the

292 next section. The $\Delta\tau$ and Δr_e can then in turn be used to estimate the uncertainties

293 and potential biases in τ and r_e retrievals due to ignoring the sub-pixel reflectance

294 variability in the bi-spectral method. Our framework can also be used to understand the

295 differences among retrievals based on instruments with different spatial resolutions.

296 　　Finally, it is worth mentioning that Eq. (8) can be rewritten in a slightly different

297 form as follows:

298

$$
\begin{pmatrix} \Delta\tau \\ \Delta r_e \end{pmatrix} \begin{pmatrix} -\dfrac{1}{2}\dfrac{\partial^2\tau\left(\overline{R_{VIS}},\overline{R_{SWIR}}\right)}{\partial R_{VIS}^2}\left(\overline{R_{VIS}}\right)^2 & -\dfrac{\partial^2\tau\left(\overline{R_{VIS}},\overline{R_{SWIR}}\right)}{\partial R_{VIS}\,\partial R_{SWIR}}\left(\overline{R_{VIS}}\cdot\overline{R_{SWIR}}\right) & -\dfrac{1}{2}\dfrac{\partial^2\tau\left(\overline{R_{VIS}},\overline{R_{SWIR}}\right)}{\partial R_{SWIR}^2}\left(\overline{R_{SWIR}}\right)^2 \\ -\dfrac{1}{2}\dfrac{\partial^2 r_e\left(\overline{R_{VIS}},\overline{R_{SWIR}}\right)}{\partial R_{VIS}^2}\left(\overline{R_{VIS}}\right)^2 & -\dfrac{\partial^2 r_e\left(\overline{R_{VIS}},\overline{R_{SWIR}}\right)}{\partial R_{VIS}\,\partial R_{SWIR}}\left(\overline{R_{VIS}}\cdot\overline{R_{SWIR}}\right) & -\dfrac{1}{2}\dfrac{\partial^2 r_e\left(\overline{R_{VIS}},\overline{R_{SWIR}}\right)}{\partial R_{SWIR}^2}\left(\overline{R_{SWIR}}\right)^2 \end{pmatrix} \begin{pmatrix} H_{\sigma_{VIS}}^2 \\ H_{cov} \\ H_{\sigma_{SWIR}}^2 \end{pmatrix}
$$

~~299~~

300

301   (9)

302   where $H_{\sigma_{VIS}}^2 = \sigma_{VIS}^2 / \left(\overline{R_{VIS}}\right)^2$, $H_{\sigma_{SWIR}}^2 = \sigma_{SWIR}^2 / \left(\overline{R_{SWIR}}\right)^2$,   and

303    $H_{COV} = \mathrm{cov}\left(R_{VIS},R_{SWIR}\right)/\left(\overline{R_{VIS}}\cdot\overline{R_{SWIR}}\right)$. Note that $H_{\sigma_{VIS}}$ has been used in previous studies

304   as an index of sub-pixel inhomogeneity, in particular for MODIS cloud retrievals [e.g.,

305   *Liang et al.*, 2009; *Di Girolamo et al.*, 2010; *Zhang and Platnick*, 2011; *Zhang et al.*, 2012;

306   *Cho et al.*, 2015]. Therefore, although Eq. (9) and (8) are equivalent, some readers may

307   find $\left(H_{\sigma_{VIS}}^2, H_{cov}, H_{\sigma_{SWIR}}^2\right)^T$ more familiar than $\left(\sigma_{VIS}^2,\ \mathrm{cov},\ \sigma_{SWIR}^2\right)^T$.

308   It is important to point out that Eqs. (8)-(9) hold, no matter whether the sub-

309   pixel reflectance variations (i.e., non-zero $\left(\sigma_{VIS}^2,\ \mathrm{cov},\ \sigma_{SWIR}^2\right)^T$) are attributable to sub-

310   pixel scale cloud property variations, 3-D radiative effects, or both. It is the

311   interpretation of the resultant $\Delta\tau$ and Δr_e that is dependent on the circumstances and

312   needs to be made with caution.

313   Finally, it is important to note that a critical assumption in our derivation is that

314   the truncation error ε in the Taylor expansion is negligible. This term is a summation of

315   all the higher order derivatives. Take r_e for example, the form of the kth order derivative:

316
$$\frac{1}{k!}\frac{d^k r_e}{dR^k} = \sum_{0 \leq m \leq k} \frac{1}{m!(k-m)!}\frac{\partial^k r_e}{\partial R_{vis}^m \partial R_{vis}^{k-m}}\left(\overline{R_{VIS}}, \overline{R_{SWIR}}\right)\Delta R_{VIS}^m \Delta R_{SWIR}^{k-m}.$$ (10)

317 Because there is no analytical solution to the higher order derivatives, we can only

318 assess the validity of this assumption and evaluate the accuracy of our framework

319 numerically, which is done in the next section.

320 **4. Numerical tests**

321 In this section, we evaluate the accuracy and limits of our mathematical framework

322 using two examples. The main objective is to assess, through case studies, if the higher

323 order derivative terms are negligible so that our framework in Eq. (8) provides an

324 accurate estimate of the PPHB.

325 4.1. Cloud fields from large-eddy simulation

326 In the first example, we test our framework using a synthetic cloud field simulated

327 from a large-eddy simulations (LES) model (DHARMA) with bin microphysics [*Ackerman*

328 *et al.*, 2004]. The LES case is based on an idealized case study [*Stevens et al.*, 2010] from

329 the Atlantic Trade Wind Experiment (ATEX), with an diagnostic treatment of aerosol,

330 specified to have a uniform number concentration of 40 cm^{-3}. The ATEX simulation

331 represents a trade-wind cumulus case under a sharp inversion. The ATEX simulation has

332 a domain size of 9.6 x 9.6 x 3 km, with a uniform horizontal grid of Δx=Δy=100 m and a

333 fixed vertical grid spacing of Δz=40 m. Further details of the model setup for the LES

334 case are provided in Zhang et al. [2012]. The droplet size distributions from the LES are

335 used to drive the radiative transfer simulations. The solar zenith and azimuth angle are

336 set at 20° and 30°, respectively, for the radiative transfer simulations. For simplicity, the

337   surface is assumed to be black. Both 1-D and 3-D radiative transfer simulations were

338   performed, using the DISORT [*Stamnes et al.*, 1988] and the I3RC model [*Pincus and*

339   *Evans*, 2009], respectively. We focus on the 3-D results because they are more

340   representative of real retrievals. The 1-D results are similar and are therefore not shown

341   here.

342   We first run radiative transfer simulations at the 100-m horizontal resolution of the

343   LES grid. Figure 5a—c show the simulated 100-m cloud bi-directional reflectances at

344   nadir viewing angle for the 0.86, 2.1, and 3.7 μm MODIS bands, receptively. Then, the

345   100m reflectances are aggregated to 400 m to simulate the coarse-resolution

346   observations, which are shown in Figure 5d—f. Obviously, for each 400-m pixel we have

347   4x4 100m pixels that can be used to derive the variances and covariances of sub-pixel

348   reflectance variances. Figure 6 shows the sub-pixel reflectance variances, $\sigma^2_{0.86}$, $\sigma^2_{2.1}$ and

349    $\sigma^2_{3.7}$, and covariances, $\mathrm{cov}(R_{0.86}, R_{2.1})$ and $\mathrm{cov}(R_{0.86}, R_{3.7})$ derived from 100-m

350   reflectances. Because of the large, order-of-magnitude differences between $R_{0.86}$, $R_{2.1}$

351   and $R_{3.7}$, $\sigma^2_{0.86}$ is substantially larger than $\sigma^2_{2.1}$, which in turn is substantially larger than

352    $\sigma^2_{3.7}$. Both covariances $\mathrm{cov}(R_{0.86}, R_{2.1})$ and $\mathrm{cov}(R_{0.86}, R_{3.7})$ are generally positive,

353   indicating a general positive correlation between SWIR and VIS/NIR band cloud

354   reflectances. This is not surprising because $R_{2.1}$ and $R_{3.7}$ do increase with τ when the

355   cloud is optically thin. Only for optically thick clouds do $R_{2.1}$ and $R_{3.7}$ become

356   independent from $R_{0.86}$. Figure 7 shows the reflectance variances and covariances

357   normalized by the mean reflectances squared, i.e., $H^2_{\sigma_{0.86}}$, $H^2_{\sigma_{2.1}}$ and $H^2_{\sigma_{3.7}}$ and

358     $\mathrm{cov}\left(R_{0.86}, R_{2.1}\right) / \left(\overline{R_{0.86}}, \overline{R_{2.1}}\right)$ and $\mathrm{cov}\left(R_{0.86}, R_{3.7}\right) / \left(\overline{R_{0.86}} \cdot \overline{R_{3.7}}\right)$. After the normalization,

359     $H^2_{\sigma_{0.86}}$, $H^2_{\sigma_{2.1}}$ and $H^2_{\sigma_{3.7}}$ are more comparable in terms of magnitude. In addition, cloud

360   edges are seen to have larger sub-pixel inhomogeneity than the center of the cloud,

361   which has also been found in MODIS observations [*Zhang and Platnick*, 2011; *Liang and*

362   *Girolamo*, 2013].

363   The τ retrievals based on the simulated 100-m cloud reflectances ($R_{0.86}$ and $R_{2.1}$

364   combination) in Figure 5a—b are shown in Figure 8a, which closely follow the $R_{0.86}$

365   observations in Figure 5a. The τ retrievals based on the $R_{0.86}$ and $R_{3.7}$ combination are

366   mostly identical and therefore not shown. The $r_{e,2.1}$ and $r_{e,3.7}$ retrievals based on the

367   100-m reflectances are shown in Figure 8b—c. For consistency with the notation in

368   Section 3, we refer to these retrievals as sub-pixel retrievals, i.e., $\tau\left(R_{0.86,i}, R_{2.1,i}\right)$,

369     $r_e\left(R_{0.86,i}, R_{2.1,i}\right)$ and $r_e\left(R_{0.86,i}, R_{3.7,i}\right)$. The τ, $r_{e,2.1}$ and $r_{e,3.7}$ retrievals based on the

370   aggregated 400m reflectances in Figure 5d—f are shown in Figure 8d—f, respectively,

371   which are referred to as pixel-level retrievals $\tau\left(\overline{R_{0.86,i}}, \overline{R_{2.1,i}}\right)$, $r_e\left(\overline{R_{0.86,i}}, \overline{R_{2.1,i}}\right)$ and

372     $r_e\left(\overline{R_{0.86,i}}, \overline{R_{3.7,i}}\right)$.

373   Having derived both sub-pixel and pixel level retrievals, we first compute the biases

374   caused by the homogenous pixel assumption, $\Delta\tau$ and Δr_e, as expressed in Eq. (3). The

375   results are shown in Figure 9a—c. It can be seen that $\Delta\tau$ is mostly negative over the

376   whole domain, as one would expect based on the PPHB. However, the Δr_e, especially

377     $\Delta r_{e,2.1}$, is predominantly positive, which is the opposite of PPHB but consistent with the

378   findings in Zhang and Platnick [2011] and Zhang et al. [2012]. It should be pointed out

379   that the cloud-free pixels are marked in black in the figure. The pixels in gray are partly

380   cloudy pixels (i.e., one or more 100-m sub-pixels are cloud-free). (Because it is uncertain

381   how cloud-free sub-pixels should be treated in the spatial averages, partly cloudy pixels

382   are excluded from our analysis.)

383   To assess the accuracy of our framework, we derived the second set of $\Delta\tau$ and Δr_e

384   based on Eq. (8) using the matrix of 2nd derivatives (Figure 3 andFigure 4) and the sub-

385   pixel reflectance variances and covariances (Figure 6). The results from this method are

386   shown in Figure 9d—f. Evidently, $\Delta\tau$ and Δr_e derived in two different and independent

387   ways agree very well. The correlation coefficients all exceed 0.8 as shown in Figure 9g—

388   i. Only those pixels with large sub-pixel inhomogeneity index $H_{\sigma_{0.86}}$ (>0.5) deviate from

389   the one-to-one line. For these pixels the higher order terms $O\left(\Delta R^3\right)$ ignored in Eq. (8),

390   likely impact $\Delta\tau$ and Δr_e. But such cases are relatively rare for this LES scene. The

391   overall excellent agreement clearly demonstrates that our framework is able to provide

392   an accurate quantitative estimation of the biases in τ and r_e retrievals caused by the

393   homogenous pixel assumption for overcast pixels.

394   An advantage of using Eq. (8) is that the bias can be further decomposed into the

395   contributions from each term in the matrix of 2nd derivatives, which help us to better

396   understand the relative importance of various factors in causing the bias. For example,

397   as   shown   in   Figure   10a—c,   the τ retrieval   bias   is   dominated   by   the

398    $-\dfrac{1}{2}\dfrac{\partial^2\tau\left(\overline{R_{VIS}},\overline{R_{SWIR}}\right)}{\partial R_{VIS}^2}\cdot\sigma_{VIS}^2$ term in Eq. (7). As mentioned before, this term corresponds to

399　　the PPHB (Figure 2a), which is why the total $\Delta\tau$ in Figure 9 is generally negative. In the

400　　case of the $r_{e,3.7}$ retrieval, both the positive $-\dfrac{1}{2}\dfrac{\partial^2 r_e\left(\overline{R_{VIS}},\overline{R_{SWIR}}\right)}{\partial R_{VIS}^2}\cdot\sigma_{VIS}^2$ term (Figure 10g)

401　　and the negative $-\dfrac{1}{2}\dfrac{\partial^2 r_e\left(\overline{R_{VIS}},\overline{R_{SWIR}}\right)}{\partial R_{SWIR}^2}\cdot\sigma_{SWIR}^2$ term (Figure 10i) are significant. The former

402　　corresponds to the example in Figure 2c, while the latter refers to the example in Figure

403　　2b. After summation, the $-\dfrac{1}{2}\dfrac{\partial^2 r_e\left(\overline{R_{VIS}},\overline{R_{SWIR}}\right)}{\partial R_{VIS}^2}\sigma_{VIS}^2$ is dominant and leads to the overall

404　　positive bias in the $r_{e,3.7}$ retrieval. The bias in the $r_{e,2.1}$ retrieval is even more

405　　complicated, as all three terms on the right hand side of Eq. (6) contribute substantially

406　　to the bias. Overall, the positive terms in Figure 10d—e dominate the total error budget,

407　　leading to a generally positive $\Delta r_{e,2.1}$ in Figure 8.

408　　　　In the above example, the solar zenith angle is high, with $\theta_0 = 20\,°$. We also tested

409　　our framework in a case with low solar zenith angle of $\theta_0 = 60\,°$ and the results are

410　　shown in Figure 11. The correlations between the biases from the numerical simulations

411　　and those predicted by our framework are substantial, suggesting our framework works

412　　equally well for a high sun in this case.

413　　　　From the above example, one can clearly see that our framework provides a

414　　comprehensive explanation of the impact of sub-pixel inhomogeneity on τ and r_e

415　　retrievals. As mentioned earlier we have also tested our framework on the retrievals

416　　based on reflectance using 1-D radiative transfer, and find the predicted $\Delta\tau$ and Δr_e

417　　based on our framework to agree very well with the numerical results (not shown).

418 We'd like to point out here that less sensitivity to sub-pixel heterogeneity in the

419 3.7μm channel should not necessarily be equated to less r_e bias in the overall retrieval.

420 For simplicity, our 3.7 μm analysis deals with reflectance only. Thus it assumes that the

421 cloud and surface temperatures are known without error, as are the atmospheric

422 emission/correction terms, needed to infer cloud top reflectance from top-of-

423 atmosphere measurements of emitted and reflected radiation. Because we are dealing

424 with reflectance only, it is implicitly assumed that the effects of sub-pixel heterogeneity

425 on the cloud temperature retrieval and atmospheric correction are negligible. The

426 validity of this assumption will be assessed in future work.

427

428 ## 4.2. MODIS retrieval test

429 In the second example, we test our framework using MODIS observations. The

430 MODIS instrument has 36 spectral bands. The spatial resolution of most bands (bands

431 8—36) is 1 km. Bands 3—7 have a 500-m resolution. Bands 1 and 2 have a 250 m spatial

432 resolution. The current (collection 06) operational MODIS cloud property retrieval

433 products, such as τ, r_e and LWP, are made at 1-km resolution. The higher spatial

434 resolution of the 0.86 μm (band 2) and 2.1 μm (band 7) sensors provides us with an

435 opportunity to test our framework and investigate the impact of sub-pixel

436 inhomogeneity on the MODIS τ and r_e retrievals. For this purpose, we selected a case

437 shown in Figure 12. The granule in Figure 12a was collected by MODIS onboard the

438 Terra satellite on September 9th 2006 over the Gulf of Mexico. We further selected a

439 small region off the coast of Louisiana marked in the red box for our test. A zoom-in

440   view of this small region at the 1km and 500m resolutions is shown in Figure 12b and

441   Figure 12c, respectively.

442   Similar to the LES example, we first developed two sets of cloud property retrievals,

443   one at a higher spatial resolution of 500 m and the other at a coarser resolution of 1 km.

444   Figure 13a and b show the 500 m resolution τ and r_e retrievals, respectively, based on

445   the combination of 0.86 and 2.1 μm reflectances for the selected region in Figure 12b.

446   The 1 km retrievals are shown in Figure 13c and d. This scene has a cloud fraction of

447   about 72%. In the center of the scene is a cluster of thick clouds with τ around 20 to 30,

448   and r_e ranging mainly between 15μm to 20μm. Note that in our framework the 500 m

449   retrievals are the sub-pixel $\tau\left(R_{VIS,i}, R_{SWIR,i}\right)$ and $r_e\left(R_{VIS,i}, R_{SWIR,i}\right)$. The 1 km retrievals are

450    $\tau\left(\overline{R_{VIS}}, \overline{R_{SWIR}}\right)$ and $r_e\left(\overline{R_{VIS}}, \overline{R_{SWIR}}\right)$. To derive the $\Delta\tau$ and Δr_e from our mathematical

451   framework in Eq. (8), we compute the sub-pixel reflectance variances and covariances

452   for every 1-km cloudy pixel from the 2x2 500-m sub-pixel reflectance observations. The

453   results are shown in Figure 14. Similar to the LES case, we find that the 0.86 and 2.1 μm

454   cloud reflectances are generally positively correlated over the thin cloud regions. The

455   correlation becomes weak (close to zero) over the thick cloud regions. These results

456   indicate that when the cloud is thin, the variability in both 0.86 and 2.1 μm bands is

457   controlled mainly by τ. The variability of 2.1 μm cloud reflectances becomes primarily

458   sensitive to r_e only when the cloud becomes optically thick.

459   The difference between the 1 km retrievals and the mean of 500 m retrievals are the

460   biases, $\Delta\tau$ and Δr_e, caused by the homogeneous pixel assumption. Figure 15a and b

461 show $\Delta\tau$ and Δr_e, respectively, based on Eq. (3). We found that $\Delta\tau$ is mainly negative

462 particularly in the regions with thick clouds, while Δr_e is mainly positive particularly in

463 the transition regions from thick to thin clouds. These results are very similar to what we

464 found in the LES scene in Figure 9. Both $\Delta\tau$ and Δr_e are shown in Figure 15c and d,

465 respectively. The $\Delta\tau$ and Δr_e predicted from Eq. (8) agree reasonably well with the

466 results derived from numerical retrievals in Figure 15a and b. The predicted $\Delta\tau$ based

467 on Eq. (9) and the numerical results have a correlation coefficient over 0.85 for all

468 cloudy pixels (over 0.95 for pixels with $\tau > 5$). The correlation coefficient for Δr_e is

469 significantly lower especially for thin clouds with $\tau < 5$. This is mainly because when the

470 cloud is thin the 2.1 μm cloud reflectances are not very sensitive to r_e. As a result, the

471 retrievals are subject to large uncertainties caused by radiative transfer model

472 uncertainties. If we limited the comparison only to clouds with $\tau > 5$, the correlation

473 coefficient is over 0.70.

474   In summary, our numerical framework work very well for the LES cases, indicating

475 that the high-order terms are mostly negligible in these cases. It also works reasonably

476 well for the real MODIS case, especially for the clouds with $\tau > 5$. For thinner clouds, it

477 is difficult to tell whether the deviation stems from higher-order terms or retrieval

478 uncertainties. Another factor to consider is that we only have four 500 m sub-pixels for

479 each 1 km pixel, which may be insufficient for deriving meaningful sub-pixel variance

480 and co-variance. As part of ongoing research, we are trying to retrieve τ and r_e from

481 the Advanced Space-borne Thermal Emission and Reflection Radiometer (ASTER) on

482 Terra. ASTER has a much greater spatial resolution than MODIS and therefore can

483   provide much richer information on small scale variability of cloud reflectance [*Zhao and*

484   *Di Girolamo*, 2006; *Wen et al.*, 2007]. We will further test our framework using ASTER

485   observations in future work.

486   **5. Summary and Discussion**

487   The impact of unresolved sub-pixel level variation of cloud reflectances is an

488   important source of uncertainty in the bi-spectral solar reflective method. In this study,

489   we develop a mathematical framework for understanding this impact and quantifying

490   the consequent biases, $\Delta\tau$ and Δr_e . We show in Eq. (8) that $\Delta\tau$ and Δr_e are

491   determined by two factors—the nonlinearity of the LUT and the inhomogeneity of

492   reflectances within the pixel. We tested our framework using LES cloud fields and real

493   MODIS observations. The results indicate that, in comparison with previous studies, our

494   framework provides a more comprehensive explanation and also a more accurate

495   estimation of the retrieval biases caused by the sub-pixel level variation of cloud

496   reflectances. Most importantly, it demonstrates that sub-pixel variations in cloud

497   reflectance can lead to both positive and negative values of Δr_e . In both the LES and

498   MODIS cases that we examined, Δr_e were dominantly positive, hence contributing to the

499   dominantly positive bias in retrieved r_e from resolved cloud variability.

500   Our framework could have several applications. For example, it can be used to

501   understand the differences between retrievals made at different spatial resolutions

502   (e.g., MODIS vs. SEVIRI) or based on different spectral reflectances (e.g., MODIS 2.1 μm

503   vs. 3.7 μm). It could also useful for estimating retrieval uncertainties. For example, the

504   retrieval uncertainty caused by sub-pixel reflectance variation in the operational 1 km

505 MODIS cloud products can be estimated based on our framework from the 500 m cloud

506 reflectances. It can also be integrated into the operational MODIS retrieval algorithm to

507 determine in real-time whether the high-resolution retrievals (e.g., from 1km to 500m)

508 are necessary for a given pixel. Another useful application is to help the trade-off studies

509 for instrument design. For example, the Ocean Color Imager (OCI) is the key instrument

510 planned for NASA's coming Pre-Aerosol, Clouds, and ocean Ecosystem mission

511 (http://decadal.gsfc.nasa.gov/pace.html). An important part of the OCI design trade-off

512 study is to determine the optimal spatial resolution for both ocean color and

513 atmospheric observations, including cloud property retrievals. Our framework would be

514 highly useful for such study.

515   Finally, we feel necessary to clarify again that our framework cannot explain or

516 predict 3-D effects, such as the illuminating, shadowing, and photon leaking, which are

517 known to substantially influence cloud reflectances and therefore retrieval results.

518 These effects are beyond the scope of this study. Our framework simply predicts the

519 statistical differences between retrievals with different spatial resolutions, regardless of

520 whether the radiative transfer is 1-D or 3-D.

521

531

References:

533 Ackerman, A. S., M. P. Kirkpatrick, D. E. Stevens, and O. B. Toon (2004), The impact of
534   humidity above stratiform clouds on indirect aerosol climate forcing, *Nature*,
535   *432*(7020), 1014–1017, doi:10.1038/nature03174.

536 Barker, H. W. (1996), A Parameterization for Computing Grid-Averaged Solar Fluxes for
537   Inhomogeneous Marine Boundary Layer Clouds. Part I: Methodology and
538   Homogeneous Biases, *JAS*, *53*(16), 2289–2303, doi:10.1175/1520-
539   0469(1996)053<2289:APFCGA>2.0.CO;2.

540 Cahalan, R. F., and J. H. Joseph (1989), Fractal statistics of cloud fields, *Monthly Weather
541   Review*, *117*(2), 261–272.

542 Cahalan, R. F., W. Ridgway, W. J. Wiscombe, T. L. Bell, and J. B. Snider (1994), The Albedo
543   of Fractal Stratocumulus Clouds, *J. Atmos. Sci.*, *51*(16), 2434–2455,
544   doi:10.1175/1520-0469(1994)051<2434:TAOFSC>2.0.CO;2.

545 Cho, H. M. et al. (2015), Frequency and causes of failed MODIS cloud property retrievals
546   for liquid phase clouds over global oceans, *Journal of Geophysical Research-
547   Atmospheres*, *120*(9), 2015JD023161–n/a, doi:10.1002/2015JD023161.

548 Davis, A., and A. Marshak (2010), 3D transport of solar radiation in clouds, *Reports on
549   Progress in Physics*.

550 Di Girolamo, L., L. Liang, and S. Platnick (2010), A global view of one-dimensional solar
551   radiative transfer through oceanic water clouds, *Geophys Res Lett*, *37*(18), L18809.

552 Dong, X., T. P. Ackerman, E. E. Clothiaux, P. Pilewskie, and Y. Han (1997), Microphysical
553   and radiative properties of boundary layer stratiform clouds deduced from
554   ground-based measurements, *J. Geophys. Res.*, *102*(D20), 23829–23843,
555   doi:10.1029/97JD02119.

556 Harshvardhan, and D. A. Randall (1985), Comments on "The Parameterization of
557   Radiation for Numerical Weather Prediction and Climate Models," *Mon. Wea. Rev*,
558   *113*(10), 1832–1833, doi:10.1175/1520-0493(1985)113<1832:COPORF>2.0.CO;2.

559 Kato, S., L. M. Hinkelman, and A. Cheng (2006), Estimate of satellite-derived cloud optical
560   thickness and effective radius errors and their effect on computed domain-averaged
561   irradiances, *J. Geophys. Res.*, *111*(D17), D17201, doi:10.1029/2005JD006668.

562 Liang, L., and L. D. Girolamo (2013), A global analysis on the view-angle dependence of
563   plane-parallel oceanic liquid water cloud optical thickness using data synergy from

564 MISR and MODIS, *Journal of Geophysical Research-Atmospheres*, *118*(5), 2389–2403,
565 doi:10.1029/2012JD018201.

566 Liang, L., L. Di Girolamo, and S. Platnick (2009), View-angle consistency in reflectance,
567 optical thickness and spherical albedo of marine water-clouds over the northeastern
568 Pacific through MISR-MODIS fusion, *Geophysical Research Letters*, *36*(9), L09811,
569 doi:10.1029/2008GL037124.

570 Liang, L., L. Di Girolamo, and W. Sun (2015), Bias in MODIS cloud drop effective radius for
571 oceanic water clouds as deduced from optical thickness variability across scattering
572 angles, *Journal of Geophysical Research-Atmospheres*, *120*(15), 7661–7681,
573 doi:10.1002/2015JD023256.

574 Marshak, A., S. Platnick, T. Várnai, G. Wen, and R. F. Cahalan (2006), Impact of
575 three-dimensional radiative effects on satellite retrievals of cloud droplet sizes, *J.*
576 *Geophys. Res.*, *111*(D9), D09207, doi:10.1029/2005JD006686.

577 Minnis, P. et al. (2011), CERES Edition-2 Cloud Property Retrievals Using TRMM VIRS and
578 Terra and Aqua MODIS Data-Part I: Algorithms, *IEEE TRANSACTIONS ON GEOSCIENCE*
579 *AND REMOTE SENSING*, *49*(11), 4374–4400, doi:10.1109/TGRS.2011.2144601.

580 Nakajima, T., and M. D. King (1990), Determination of the Optical Thickness and Effective
581 Particle Radius of Clouds from Reflected Solar Radiation Measurements. Part I:
582 Theory, *J. Atmos. Sci.*, *47*(15), 1878–1893, doi:10.1175/1520-
583 0469(1990)047<1878:DOTOTA>2.0.CO;2.

584 Oreopoulos, L., and R. Davies (1998), Plane Parallel Albedo Biases from Satellite
585 Observations. Part I: Dependence on Resolution and Other Factors, *Journal of*
586 *Climate*, *11*(5), 919–932.

587 Oreopoulos, L., R. F. Cahalan, and S. Platnick (2007), The Plane-Parallel Albedo Bias of
588 Liquid Clouds from MODIS Observations, *Journal of Climate*, *20*(20), 5114–5125,
589 doi:10.1175/JCLI4305.1.

590 Painemal, D., and P. Zuidema (2011), Assessment of MODIS cloud effective radius and
591 optical thickness retrievals over the Southeast Pacific with VOCALS-REx in situ
592 measurements, *J Geophys Res*, *116*(D24), D24206.

593 Pincus, R., and K. F. Evans (2009), Computational Cost and Accuracy in Calculating Three-
594 Dimensional Radiative Transfer: Results for New Implementations of Monte Carlo and
595 SHDOM,, *66*(10), 3131–3146, doi:10.1175/2009JAS3137.1.

596 Pincus, R., S. A. McFarlane, and S. A. Klein (1999), Albedo bias and the horizontal

597   variability of clouds in subtropical marine boundary layers: Observations from ships
598   and satellites, *J. Geophys. Res.*, *104*(D6), 6183–6191, doi:10.1029/1998JD200125.

599 Platnick, S., M. D. King, S. A. Ackerman, W. P. Menzel, B. A. Baum, J. C. Riédi, and R. A.
600   Frey (2003), The MODIS cloud products: algorithms and examples from Terra, *IEEE*
601   *TRANSACTIONS ON GEOSCIENCE AND REMOTE SENSING*, *41*(2), 459–473,
602   doi:10.1109/TGRS.2002.808301.

603 Roebeling, R., A. Feijt, and P. Stammes (2006), Cloud property retrievals for climate
604   monitoring: Implications of differences between Spinning Enhanced Visible and
605   Infrared Imager (SEVIRI) on METEOSAT-8 and Advanced Very High Resolution
606   Radiometer (AVHRR) on NOAA-17, *J Geophys Res*, *111*, D20210.

607 Stamnes, K., S. Tsay, K. Jayaweera, and W. Wiscombe (1988), Numerically stable
608   algorithm for discrete-ordinate-method radiative transfer in multiple scattering and
609   emitting layered media,, *27*(12), 2502–2509.

610 Stevens, D. E., A. S. Ackerman, and C. S. Bretherton (2010), Effects of Domain Size and
611   Numerical Resolution on the Simulation of Shallow Cumulus Convection,
612   *http://dx.doi.org/10.1175/1520-0469(2002)059<3285:EODSAN>2.0.CO;2*, *59*(23),
613   3285–3301, doi:10.1175/1520-0469(2002)059<3285:EODSAN>2.0.CO;2.

614 Várnai, T., and A. Marshak (2002), Observations of Three-Dimensional Radiative Effects
615   that Influence MODIS Cloud Optical Thickness Retrievals, *J. Atmos. Sci.*, *59*(9), 1607–
616   1618, doi:10.1175/1520-0469(2002)059<1607:OOTDRE>2.0.CO;2.

617 Walther, A., and A. K. Heidinger (2012), Implementation of the Daytime Cloud Optical and
618   Microphysical Properties Algorithm (DCOMP) in PATMOS-x, *J. Appl. Meteor.*
619   *Climatol.*, *51*(7), 1371–1390, doi:10.1175/JAMC-D-11-0108.1.

620 Wen, G., A. Marshak, R. F. Cahalan, L. A. Remer, and R. G. Kleidman (2007), 3-D
621   aerosol-cloud radiative interaction observed in collocated MODIS and ASTER images
622   of cumulus cloud fields, *J. Geophys. Res.*, *112*(D13).

623 Zhang, Z. (2013), On the sensitivity of cloud effective radius retrieval based on spectral
624   method to bi-modal droplet size distribution: A semi-analytical model, *Journal of*
625   *Quantitative Spectroscopy and Radiative Transfer VL -*, (0 SP - EP - PY - T2 -),
626   doi:10.1016/j.jqsrt.2013.05.033.

627 Zhang, Z., A. S. Ackerman, G. Feingold, S. Platnick, R. Pincus, and H. Xue (2012), Effects of
628   cloud horizontal inhomogeneity and drizzle on remote sensing of cloud droplet
629   effective radius: Case studies based on large-eddy simulations, *J Geophys Res*,
630   *117*(D19), D19208–, doi:10.1029/2012JD017655.

631 Zhang, Z., and S. Platnick (2011), An assessment of differences between cloud effective
632   particle radius retrievals for marine water clouds from three MODIS spectral bands, *J
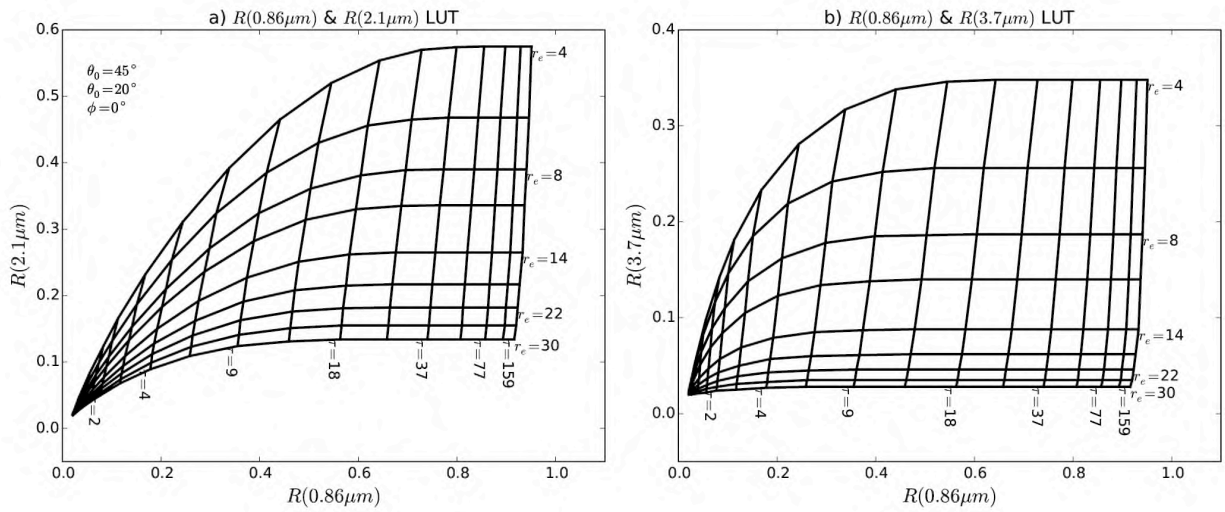633   Geophys Res*, *116*(D20), D20215, doi:10.1029/2011JD016216.

634 Zhao, G., and L. Di Girolamo (2006), Cloud fraction errors for trade wind cumuli from
635   EOS-Terra instruments, *Geophysical Research Letters*, *33*(20), L20802,
636   doi:10.1029/2006GL027088.

637

638

640

641
642   Figure 1 Examples of the look-up table of cloud bi-directional reflection function as functions of
643   cloud optical thickness and effective radius, based on the combination of a) 0.86 and 2.1 μm
644   bands, and b) 0.86 and 3.7 μm bands. Surface is assumed to be Lambertian with a reflectance of
645   0.02. Solar and viewing zenith angle are 45° and 20°, respectively. Relative azimuthal angle is 0°.

646

647
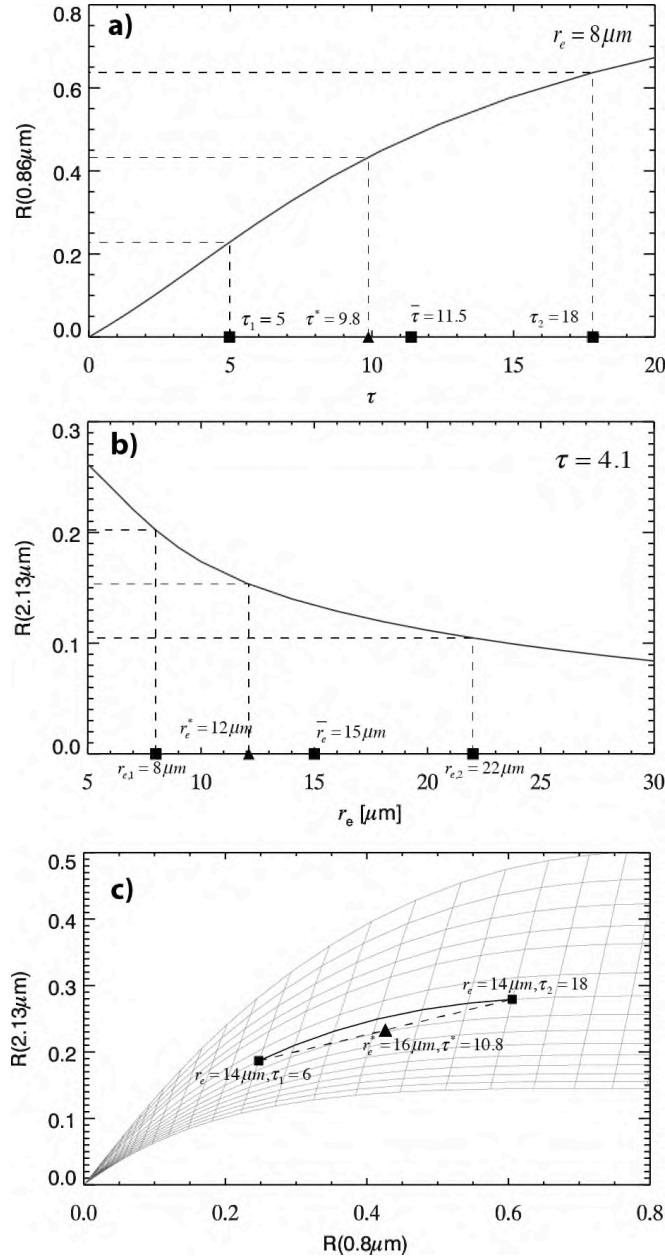
648

649   Figure 2 a) an example to illustrate the PPHB bias proposed in Cahalan et al. [1994] for τ
650   retrieval, b) example to illustrate the PPHB bias proposed in Marshak et al. [2006], c) example
651   to illustrate the r_e retrieval bias caused by sub-pixel τ variability proposed in Zhang and
652   Platnick [2011] and Zhang et al. [2012]. See text for details. Solar and view zenith angles are
653   assume to be 20° and 0° and relative azimuth angle is assumed to be 30° in these cases.

654
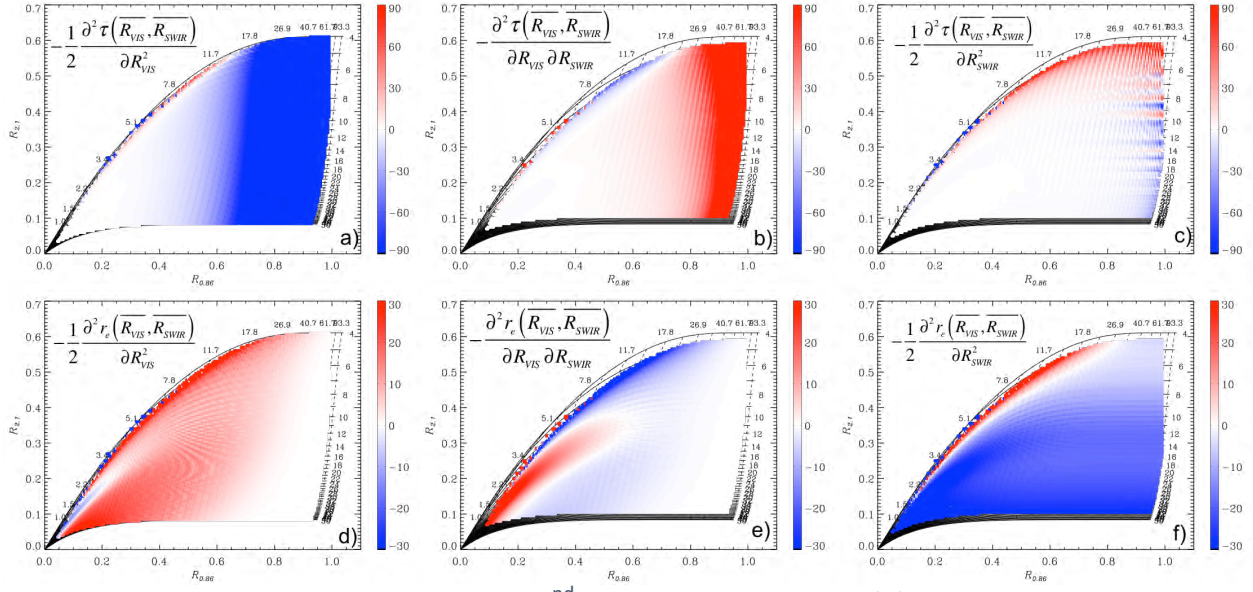
Figure 3 The sign and magnitude of each 2nd derivative term in Eq. *(8)* derived from the $R_{0.86}$ and R2.1 LUT. a) corresponds to $-\frac{1}{2}\frac{\partial^2 \tau\left(\overline{R_{VIS}},\overline{R_{SWIR}}\right)}{\partial R_{VIS}^2}$, b) to $-\frac{\partial^2 \tau\left(\overline{R_{VIS}},\overline{R_{SWIR}}\right)}{\partial R_{VIS}\,\partial R_{SWIR}}$, c) to $-\frac{1}{2}\frac{\partial^2 \tau\left(\overline{R_{VIS}},\overline{R_{SWIR}}\right)}{\partial R_{SWIR}^2}$, d) to $-\frac{1}{2}\frac{\partial^2 r_e\left(\overline{R_{VIS}},\overline{R_{SWIR}}\right)}{\partial R_{VIS}^2}$, e) to $-\frac{\partial^2 r_e\left(\overline{R_{VIS}},\overline{R_{SWIR}}\right)}{\partial R_{VIS}\,\partial R_{SWIR}}$, and f) to $-\frac{1}{2}\frac{\partial^2 r_e\left(\overline{R_{VIS}},\overline{R_{SWIR}}\right)}{\partial R_{SWIR}^2}$.

Solar and view zenith angles are assumed to be 20° and 0°, relative azimuth angle is assumed to be 30° in these cases.
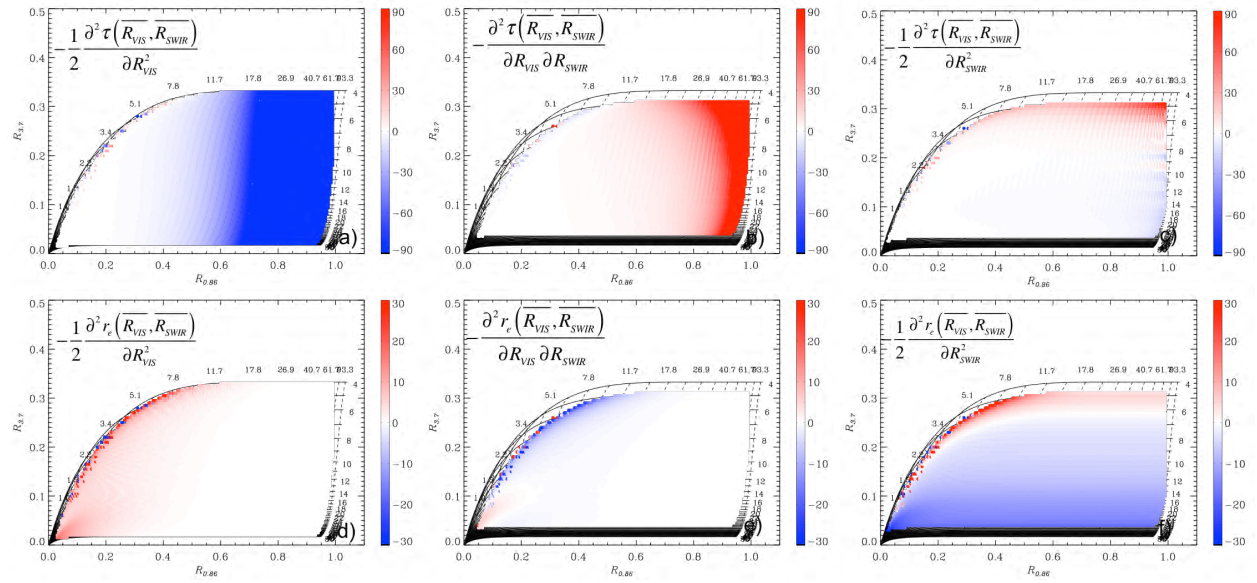
662
663 Figure 4 Same as Figure 3 , except for the $R_{0.86}$ and $R_{3.7}$ LUT. Solar and view zenith angles are
664 assume to be 20° and 0° and relative azimuth angle is assumed to be 30° in these cases.

665

666
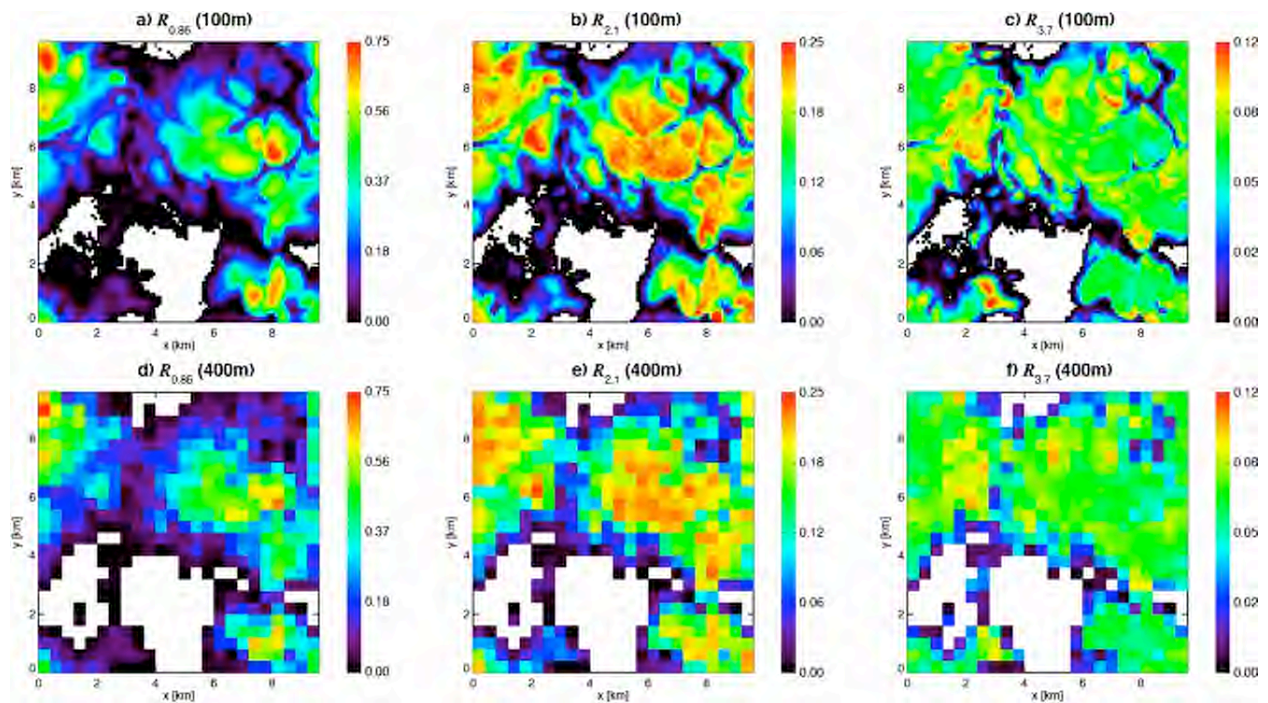
667
668   Figure 5 Simulated a) 0.86 μm, b) 2.1 μm and c) 3.7 μm MODIS bi-directional reflectances at
669   100-m resolution for the LES cloud field. d)—f) 400-m bi-directional reflectances averaged from
670   100-m resolution simulations.

671

672

673
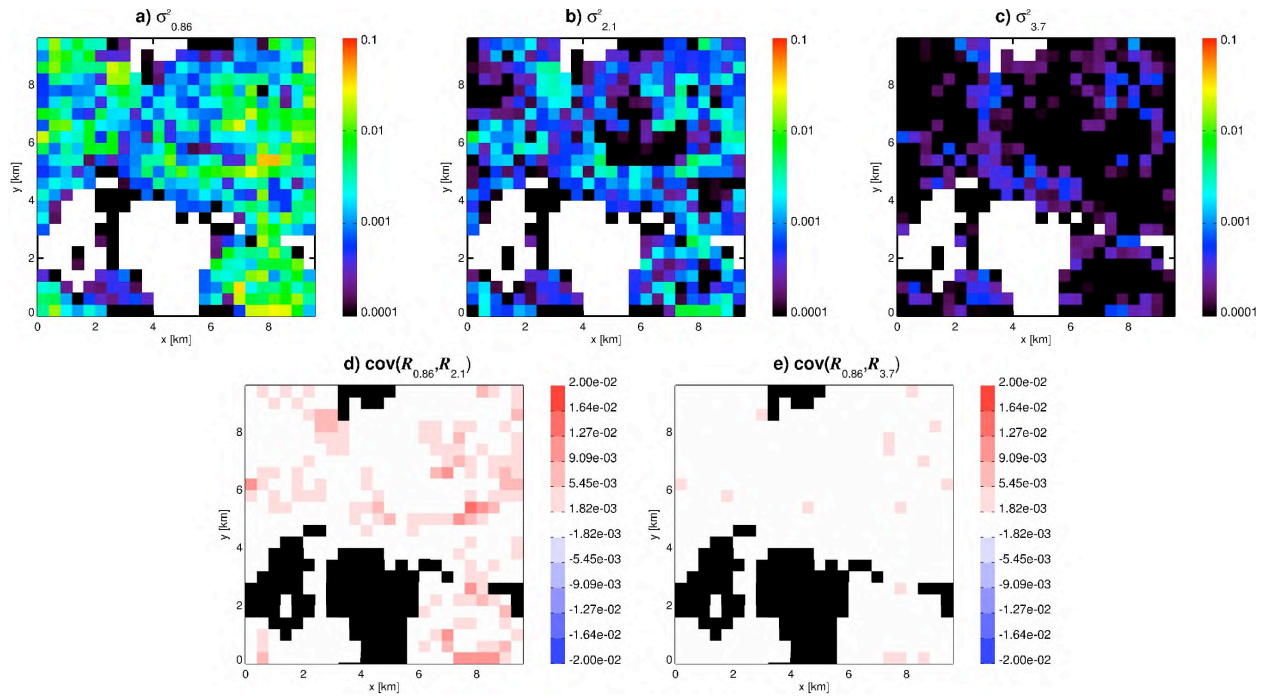
Figure 6 The sub-pixel reflectance variance a) $\sigma^2_{0.86}$, b) $\sigma^2_{2.1}$, c) $\sigma^2_{3.7}$ and covariances d) $\mathrm{cov}\left(R_{0.86}, R_{2.1}\right)$ and e) $\mathrm{cov}\left(R_{0.86}, R_{3.7}\right)$ for the LES case in Figure 5.

676
677
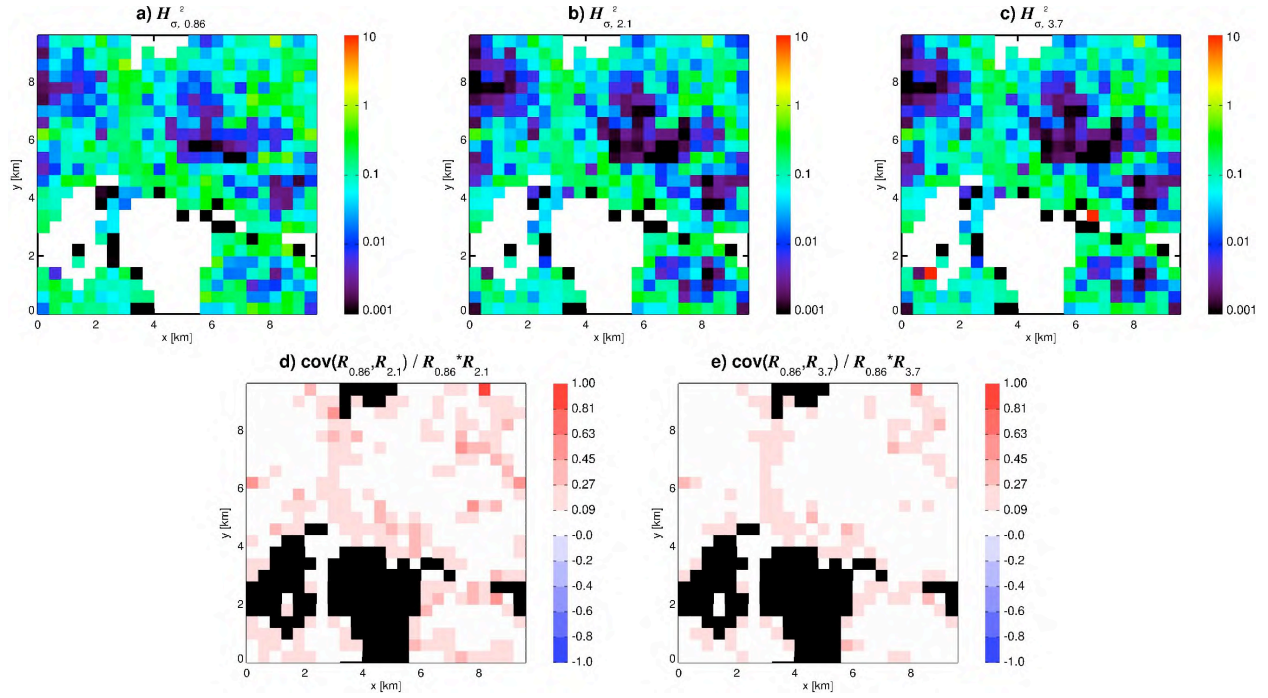
678
679 Figure 7 The sub-pixel a) $H^2_{\sigma_{0.86}}$, b) $H^2_{\sigma_{2.1}}$, c) $H^2_{\sigma_{3.7}}$ d) $\mathrm{cov}\left(R_{0.86}, R_{2.1}\right) / \left(\overline{R_{0.86}}, \overline{R_{2.1}}\right)$ and e)

680 $\mathrm{cov}\left(R_{0.86}, R_{3.7}\right) / \left(\overline{R_{0.86}}, \overline{R_{3.7}}\right)$ for the LES case in Figure 5.

681

682

683

684
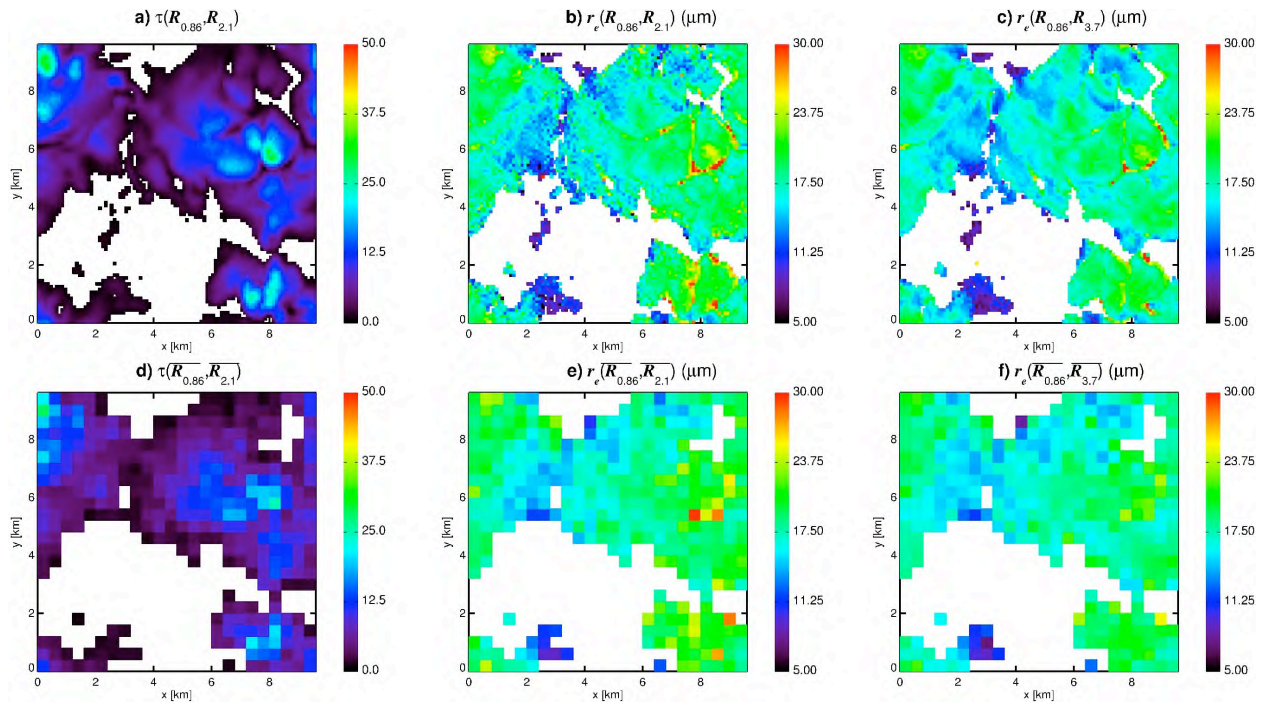
Figure 8 a) τ , b) $r_{e,2.1}$ and c) $r_{e,3.7}$ retrievals based on the 100 m reflectance. d)—f) retrievals based on the 400 m reflectance.

687

688
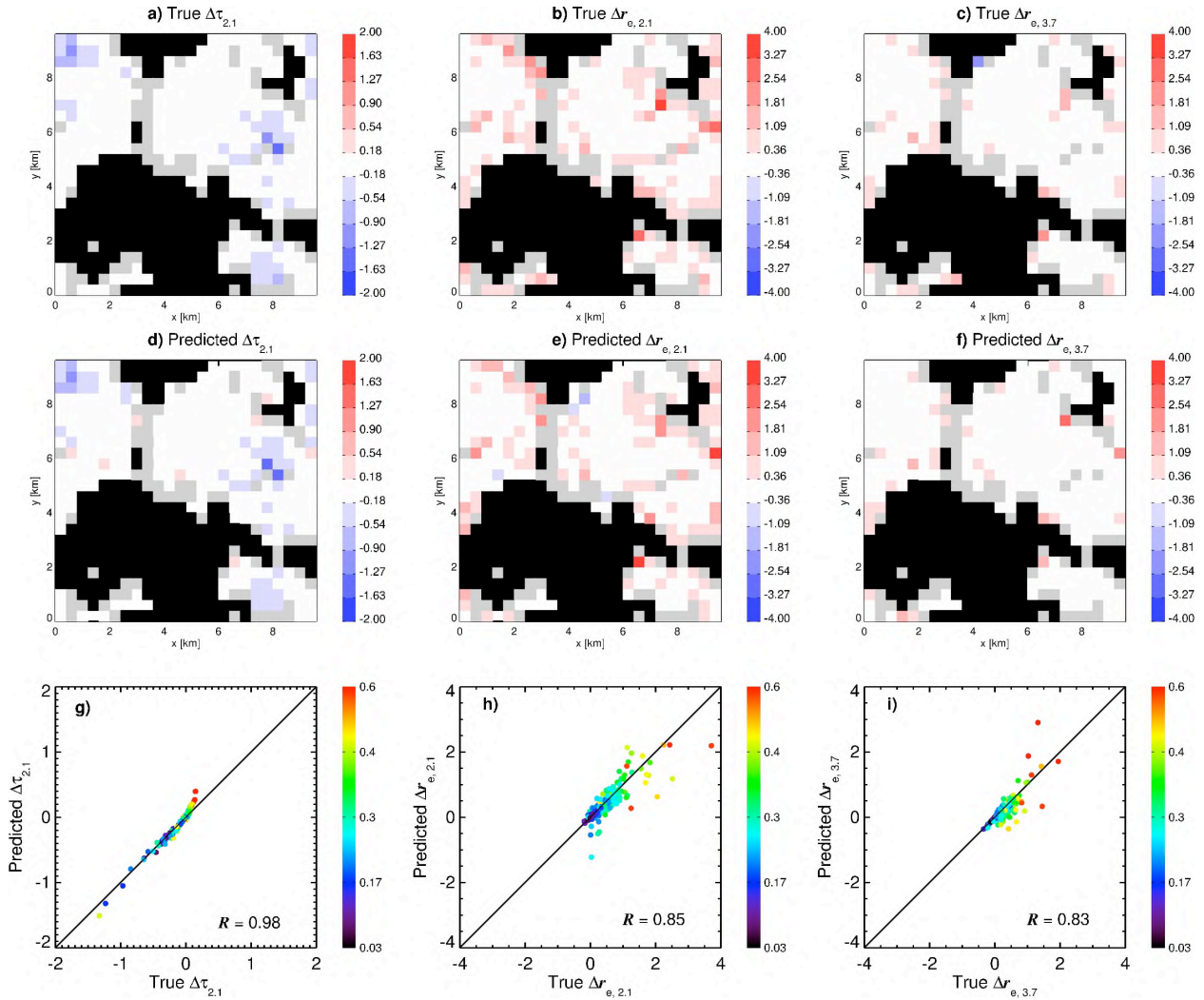
689
690 Figure 9 The a) $\Delta\tau$, b) $\Delta r_{e,2.1}$ and c) $\Delta r_{e,3.7}$ derived based on the Eq. (3). The corresponding

691 results obtained based on Eq. (8) are shown in d)—f). The pixel-to-pixel comparisons are shown

692 in g)—i), in which the color indicate the value of the sub-pixel inhomogeneity index $H_{\sigma_{0.86}}$.

693

694

a) $\Delta\tau_{2.1}$ Term 1 **b)** $\Delta\tau_{2.1}$ Term 2 **c)** $\Delta\tau_{2.1}$ Term 3

d) $\Delta r_{e,2.1}$ Term 1 **e)** $\Delta r_{e,2.1}$ Term 2 **f)** $\Delta r_{e,2.1}$ Term 3

g) $\Delta r_{e,3.7}$ Term 1 **h)** $\Delta r_{e,3.7}$ Term 2 **i)** $\Delta r_{e,3.7}$ Term 3
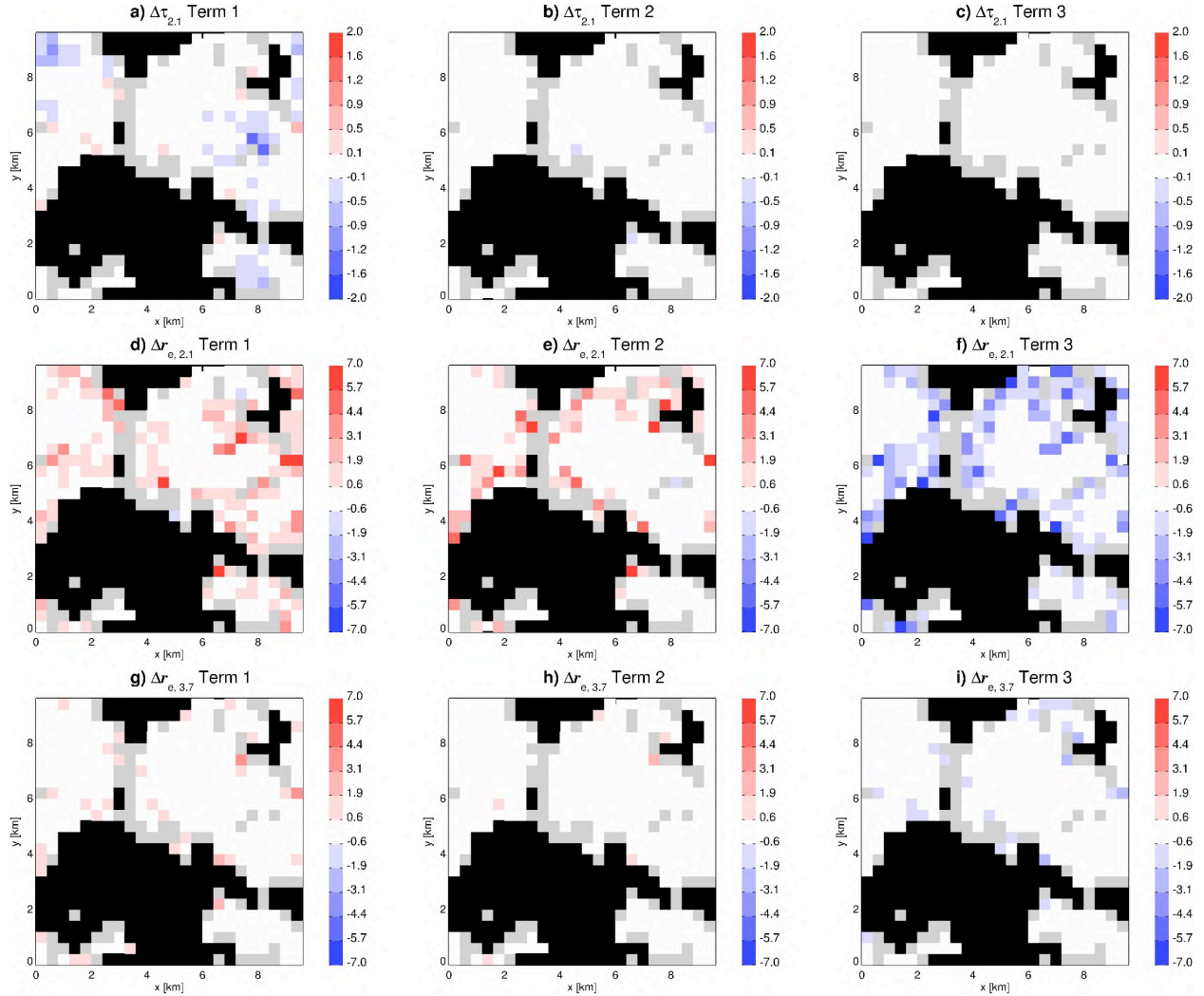
696
697 Figure 10 The decomposition of $\Delta\tau$ and Δr_e into the contributions from each term in the

698 matrix of 2nd derivative. **a)** contribution of $-\dfrac{1}{2}\dfrac{\partial^2\tau\left(\overline{R_{0.86}},\overline{R_{2.1}}\right)}{\partial R_{0.86}^2}\cdot\sigma_{0.86}^2$ to $\Delta\tau$, **b)** contribution of

699 $-\dfrac{1}{2}\dfrac{\partial^2\tau\left(\overline{R_{0.86}},\overline{R_{2.1}}\right)}{\partial R_{0.86}\partial R_{2.1}}\cdot\text{cov}\left(R_{0.86},R_{2.1}\right)$ to $\Delta\tau$, **c)** contribution of $-\dfrac{1}{2}\dfrac{\partial^2\tau\left(\overline{R_{0.86}},\overline{R_{2.1}}\right)}{\partial R_{2.1}^2}\cdot\sigma_{2.1}^2$ to $\Delta\tau$. **d)**

700 contribution of $-\dfrac{1}{2}\dfrac{\partial^2 r_e\left(\overline{R_{0.86}},\overline{R_{2.1}}\right)}{\partial R_{0.86}^2}\cdot\sigma_{0.86}^2$ to $\Delta r_{e,2.1}$, **e)** contribution of
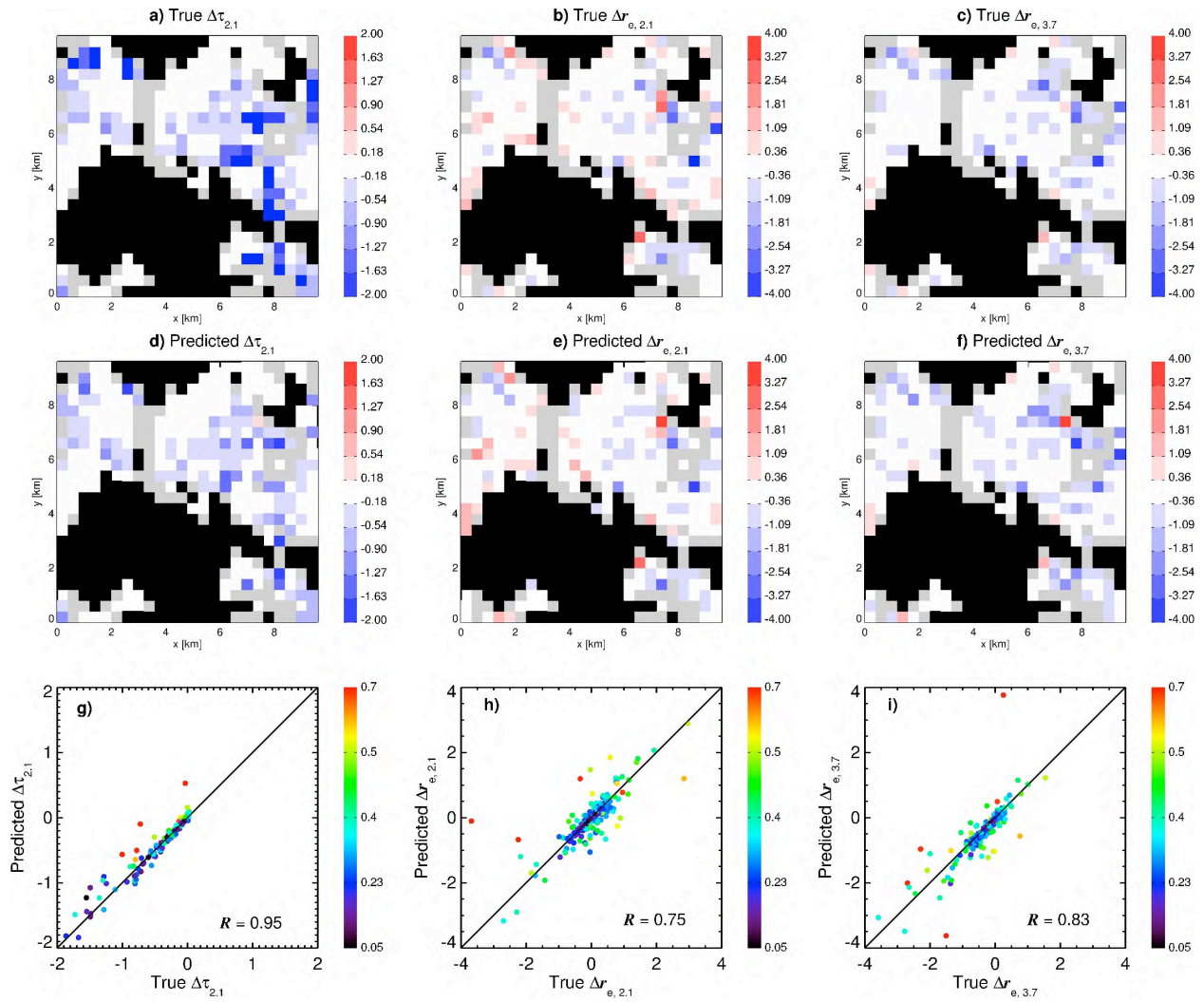
701 $-\dfrac{1}{2}\dfrac{\partial^2 r_e\left(\overline{R_{0.86}},\overline{R_{2.1}}\right)}{\partial R_{0.86}\partial R_{2.1}}\cdot\text{cov}\left(R_{0.86},R_{2.1}\right)$ to $\Delta r_{e,2.1}$, **f)** contribution of $-\dfrac{1}{2}\dfrac{\partial^2 r_e\left(\overline{R_{0.86}},\overline{R_{2.1}}\right)}{\partial R_{2.1}^2}\cdot\sigma_{2.1}^2$ to $\Delta r_{e,2.1}$. **g)**

702   contribution of $-\dfrac{1}{2}\dfrac{\partial^{2}\tau\left(\overline{R_{0.86}},\overline{R_{3.7}}\right)}{\partial R_{3.7}^{2}}\cdot\sigma_{3.7}^{2}$ to $\Delta r_{e,3.7}$. **h)** contribution of
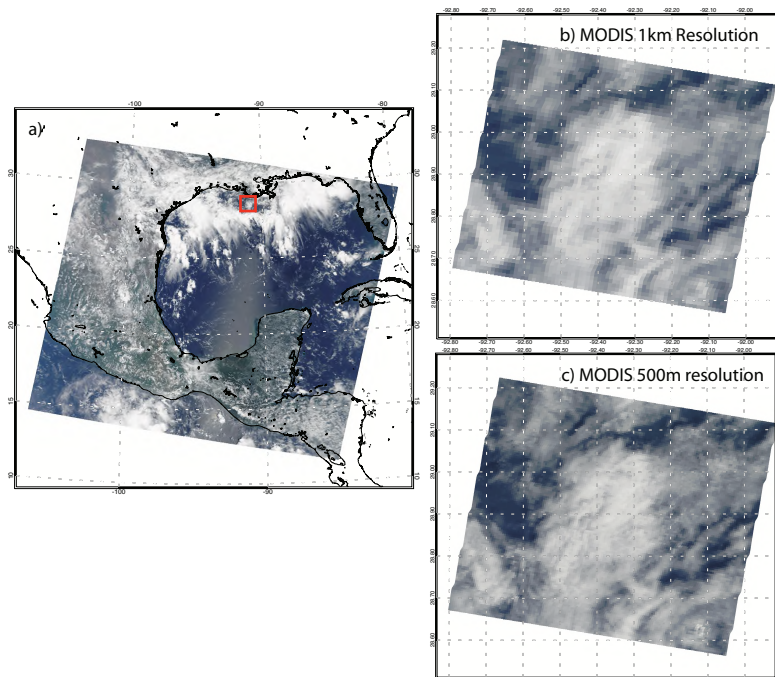
703    $-\dfrac{1}{2}\dfrac{\partial^{2}r_{e}\left(\overline{R_{0.86}},\overline{R_{3.7}}\right)}{\partial R_{0.86}\,\partial R_{3.7}}\cdot\mathrm{cov}\left(R_{0.86},R_{3.7}\right)$ to $\Delta r_{e,3.7}$, **f)** contribution of $-\dfrac{1}{2}\dfrac{\partial^{2}r_{e}\left(\overline{R_{0.86}},\overline{R_{3.7}}\right)}{\partial R_{3.7}^{2}}\cdot\sigma_{3.7}^{2}$ to $\Delta r_{e,2.1}$.

704

706
707 Figure 11 Same as Figure 9, except that in this case the solar zenith angle is 60°.
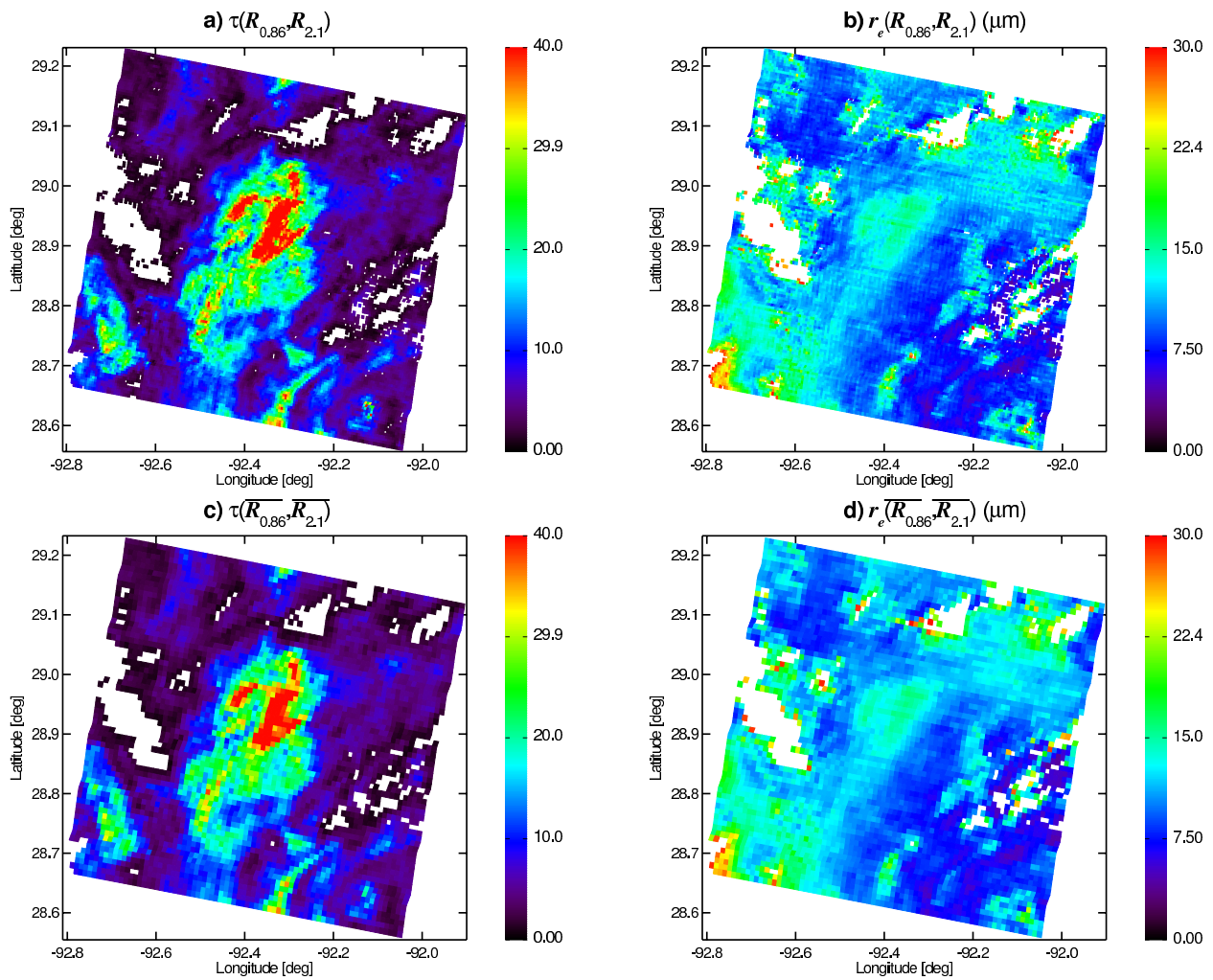
708
709

710

711
712 Figure 12 The a) RGB image of a MODIS granule collected on September 9th 2006 over the Gulf
713 of Mexico. A zoom-in view of the region in the red box based on b) 1 km MODIS true color RGB
714 image and c) 500 m MODIS true color RGB image..

715

718   Figure 13 τ and $r_{e,2.1}$ retrievals for the region in Figure 12b at the 500 m (a) and b)) and 1 km (c)
719   and d)) resolutions. The differences between 1km retrievals and the aggregated 500m retrievals
720   , i.e., $\Delta\tau$ and $\Delta r_{e,2.1}$, are shown in e) and f).
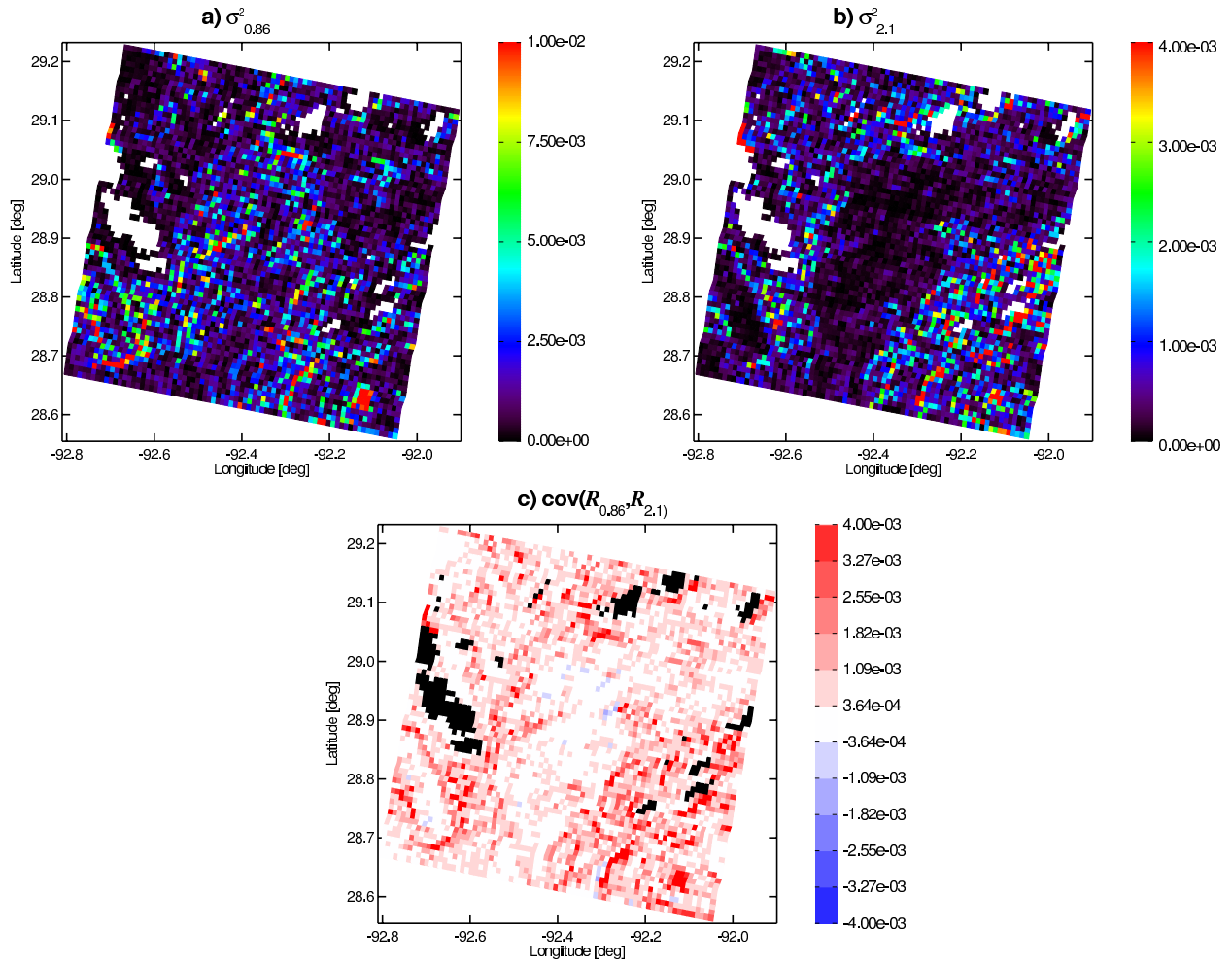
721

722
723 Figure 14 The sub-pixel reflectance variances a) $\sigma^2_{0.86}$, b) $\sigma^2_{2.1}$, and covariances c)
724 $\mathrm{cov}\left(R_{0.86}, R_{2.1}\right)$ for the MODIS case in Figure 12b.
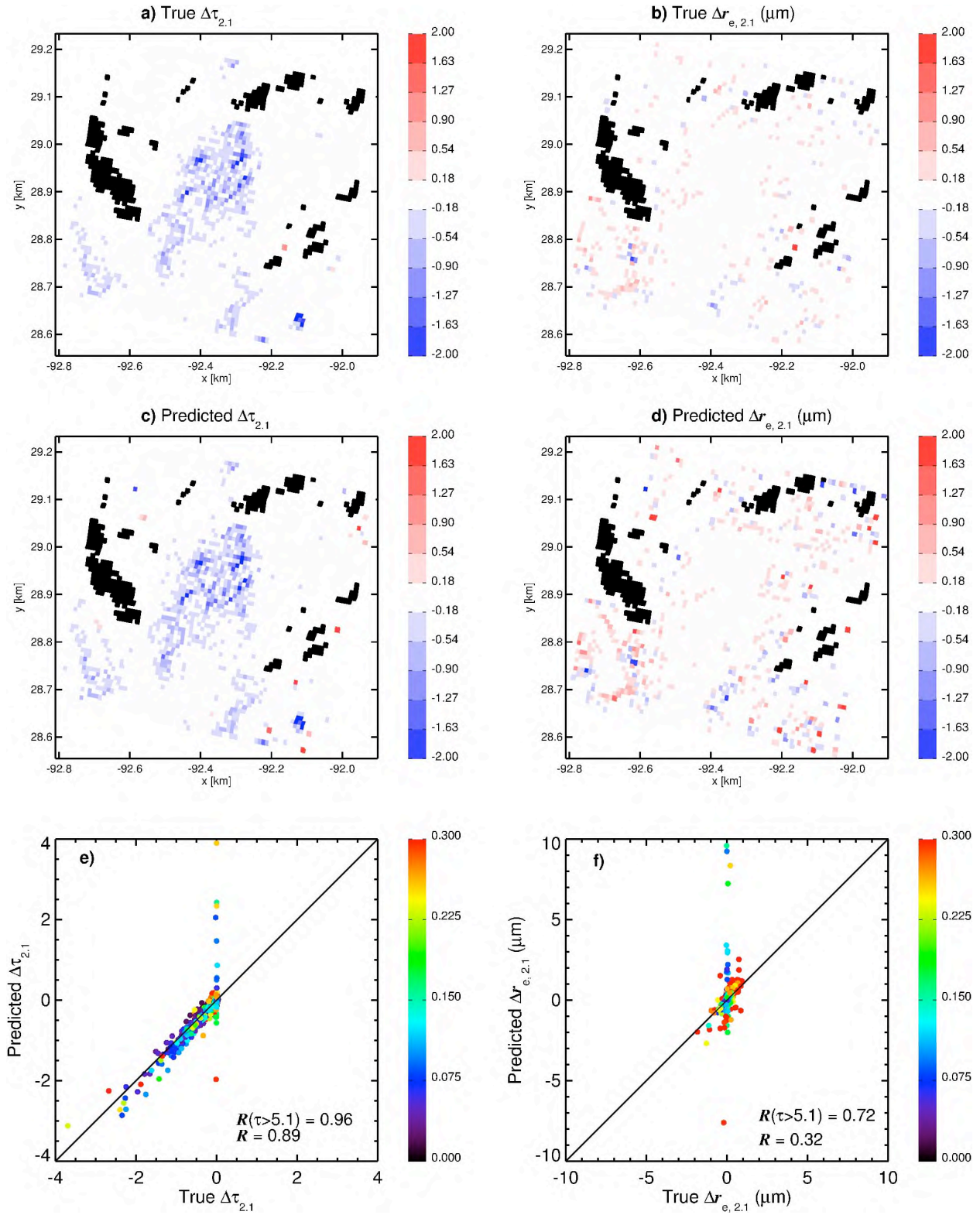
725

726

727
728 Figure 15 The a) $\Delta\tau$ and b) Δr_e derived based on the Eq. (3). The corresponding results based
729 on Eq. (8) are shown in c) and d) and comparisons in e) and f).